

# *IET Renewable Power Generation*

## Special Issue Call for Papers

---

**Be Seen. Be Cited.  
Submit your work to a new  
IET special issue**

Connect with researchers and  
experts in your field and  
share knowledge.

Be part of the latest research  
trends, faster.

[Read more](#)



The Institution of  
Engineering and Technology

# Considerations on prediction horizon and dissipative losses for wave energy converters

Zahra Shahroozi<sup>1</sup>  | Malin Göteman<sup>1</sup> | Jens Engström<sup>1</sup> | Jørgen Hals Todalshaug<sup>2</sup> 

<sup>1</sup> Department of Electrical Engineering, Uppsala University, Uppsala, Sweden

<sup>2</sup> CorPowerOcean AB, Hågersten, Sweden

## Correspondence

Zahra Shahroozi, Box 65, 751 03 Uppsala, Sweden.  
Email: zahra.shahroozi@angstrom.uu.se

## Funding information

Energimyndigheten, Grant/Award Number: Nextwave project; Svenska Forskningsrådet Formas, Grant/Award Number: 2020-03634

## Abstract

The non-causal optimal control law for wave energy converters leads to a requirement of predicting waves and wave forces over a future horizon. Using examples of generic body shapes and oscillation modes, the authors show through computations of the velocity reference trajectory how the length of prediction horizon required to reach the maximum power output depends on the level of dissipative losses in the conversion chain. The sensitivity to noise is discussed, and so is the use of filtering to improve performance when the available prediction horizon is short or predictions are inaccurate. Considerations are also made for amplitude constraints and other effects encountered in a real system. With realistic assumptions for the level of dissipative losses, results indicate that the prediction horizon needed to approach the maximum achievable power output for real systems ranges from only a few seconds up to about half a wave period, which is shorter than that has generally been assumed earlier.

## 1 | INTRODUCTION

Early wave energy research revealed the frequency domain relationships for optimal conversion of ocean wave energy to useful forms [1, 2].

However, the conversion of these relations to the time domain results in non-causal impulse response functions [1–3], and convolution terms that can only be evaluated with future knowledge of the wave elevation, excitation force or device motion [2–5].

The question of how to obtain the required future information has been addressed by many authors. Falnes [1] emphasised the importance of the memory kernel, i.e. the inverse Fourier transform of the radiation impedance, in identifying the required prediction horizon. This was further studied by Fusco and Ringwood [6] who quantified the required horizon for different sizes of floating spheres and cylinders working in the heave mode. In Price et al. [7], the coherence of ocean waves was discussed, and a clear distinction between remote and local monitoring was made for gathering the necessary wave information to feed an optimal control algorithm. The authors also introduced the premonition time; the time difference between required horizon and the coherence time based on available

monitoring of the waves. Furthermore, Mérigaud and Ringwood [8] provided an excellent review of the stochastic representation of ocean waves, and showed how an optimal predictor can be constructed based on a chosen combination of remote and local monitoring points.

The main contribution of the current paper is to investigate how dissipative losses in the system influence the limits of maximum power output under optimal control. The work is heavily inspired by the mentioned work of Fusco and Ringwood [6]. Based on a thorough analysis of the dynamic properties of the system, they computed the capture width ratio as function of the prediction horizon, and also introduced a filtering of the optimal transfer function to reduce the prediction requirement that is further studied here. However, although they did identify the radiation damping as the governing parameter for the prediction requirements, they did not provide an analysis of the effect of damping due to losses. This is provided here, and the investigation is extended to a selection of generic concepts for wave energy conversion: A spherical body oscillating in surge or heave, floating or submerged, and a bottom-hinged oscillating flap. Most proposed concepts for the harvesting of wave energy by oscillating bodies are covered by, or may be seen as a combination of these generic concepts. Even the

This is an open access article under the terms of the [Creative Commons Attribution](https://creativecommons.org/licenses/by/4.0/) License, which permits use, distribution and reproduction in any medium, provided the original work is properly cited.

© 2021 The Authors. *IET Renewable Power Generation* published by John Wiley & Sons Ltd on behalf of The Institution of Engineering and Technology

hydrodynamic behaviour and prediction requirements for oscillating water columns (OWCs) may be anticipated from the study of these concepts, as OWCs share with the floating sphere in heave the property of being source mode wave radiators. Assuming a JONSWAP spectrum for the incident waves, the sensitivity to sea state parameters and prediction accuracy is also studied. Note that the discussion of prediction algorithms is not in the scope of the paper, however, the reader is encouraged to find more information about this in [9–14].

The remainder of the paper is structured as follows; In Section 2, the theory behind the system dynamics and computation of useful power as function of available prediction horizon and loss coefficient is explained in detail. In Section 3, the chosen generic concepts are defined, and their hydrodynamic properties are described. The results of the required prediction horizon and its sensitivity to the system loss, energy period, prediction accuracy, shape factor and amplitude constraint are given in Section 4. The discussion of the results follows in Section 5, before conclusions are summarised in Section 6.

## 2 | THEORY

This section presents the equation of motion for a single-mode wave energy converter, and summarises the corresponding properties of optimal velocity for maximum power output.

### 2.1 | Time domain model

The equation of motion for a single-mode wave energy converter with position  $\eta(t)$  and velocity  $\nu(t) = \dot{\eta}(t)$  can in the time domain be written as [1],

$$(M + M_\infty)\dot{\nu}(t) + \int_0^t \nu(\tau)k(t - \tau)d\tau + R_l\nu(t) + S_b\eta(t) = F_{\text{exc}}(t) + F_{\text{PTO}}(t), \quad (1)$$

where  $F_{\text{exc}}(t)$  is the wave excitation force and  $F_{\text{PTO}}(t)$  is the power take-off (PTO) force that is used to convert the mechanical energy to useful energy. Note that  $F_{\text{PTO}}(t)$  excludes machinery losses, which are included in the loss term  $R_l\nu(t)$ . The dissipative loss coefficient  $R_l$  represents the total losses, which for the sake of simplicity and for maintaining the focus of this paper have been linearised, and which typically include hydrodynamic drag, machinery friction and flow losses. The linearisation results in the loss term being proportional to the velocity. Furthermore,  $M$  is the mass of the wave-absorbing body,  $M_\infty$  is the limit of added mass at infinite frequency and  $S_b$  is the hydrostatic stiffness coefficient.

For a rotational mode with rotation angle  $\eta(t) = \theta(t)$  and angular velocity  $\nu(t) = \dot{\theta}(t)$ , the same equation is valid provided excitation and PTO forces are replaced by the corresponding torques  $\tau_{\text{exc}}(t)$  and  $\tau_{\text{PTO}}(t)$ , and mass, damping and stiffness are replaced by moment of inertia  $I_\theta$ , angular damping  $R_\theta$  and

angular stiffness  $S_\theta$ . Moreover, it is assumed that  $\theta$  is small, i.e.  $-30^\circ < \theta < +30^\circ$ , for the following reasons [15]:

- The buoyancy restoring coefficient remains constant for small angles.
- Due to the effect of wave torque decoupling, the hydrodynamic coefficients such as radiation resistance and added inertia are independent of angular position.

Equivalent linearisation [15–17] may be used to represent loss terms like viscous drag, Coulomb friction and pressure drop over orifices in this linearised model.

### 2.2 | Frequency domain model

In the frequency domain, the equation of motion can be expressed as

$$\left( j\omega M + Z_r(\omega) + \frac{S_b}{j\omega} \right) \mathcal{V}(\omega) + R_l \mathcal{V}(\omega) = F_{\text{exc}}(\omega) + F_{\text{PTO}}(\omega), \quad (2)$$

where  $Z_r(\omega)$  is the radiation impedance due to radiated waves from the body's motion. It can be decomposed as

$$Z_r(\omega) = R_r(\omega) + j\omega M_r(\omega) = R_r(\omega) + j\omega[M_a(\omega) + M_\infty], \quad (3)$$

where  $R_r(\omega)$  is the radiation resistance, also called radiation or wave *damping*, which is a real and even function in the frequency domain, and consequently, the corresponding impulse response function is also real and even. Furthermore,  $M_a$  is the added mass less its limit when the frequency goes to infinity,  $M_\infty$ , which will then cancel out the singularity of the total added mass  $M_r(\omega)$  at infinite frequency. The equation of motion, (2), can be written in a compact form of:

$$\mathcal{V}(\omega) = \frac{1}{Z_i(\omega)} (F_{\text{PTO}}(\omega) + F_{\text{exc}}(\omega)), \quad (4)$$

where  $Z_i(\omega)$  is the intrinsic impedance and can be defined as

$$Z_i(\omega) = j\omega M + Z_r(\omega) + R_l + \frac{S_b}{j\omega}, \quad (5)$$

$$= R_r(\omega) + R_l + j \left( \omega(M + M_r(\omega)) - \frac{S_b}{\omega} \right), \quad (6)$$

$$= R_r(\omega) + jX_i(\omega). \quad (7)$$

Furthermore, the PTO force is written:

$$F_{\text{PTO}}(\omega) = Z_u(\omega)\mathcal{V}(\omega), \quad (8)$$



where  $Z_u(\omega)$  is the load impedance. Here, the definition of passive and reactive control can be distinguished as follows: in passive control, the PTO force is applied in a pure braking fashion, such that the optimum condition becomes  $Z_u(\omega) = -|Z_i(\omega)| = -\sqrt{R_i^2(\omega) + X_i^2(\omega)}$ , while reactive control allows for power reversal and use of reactive power, where the optimum is characterised by impedance matching,  $Z_u(\omega) = -Z_i^*(\omega)$  where  $*$  denotes complex conjugate. The maximum average absorbed power achieved by reactive control is usually considerably larger than passive control [1, 18, 19].

Based on this, the optimal velocity for the maximum wave energy extraction becomes [4]:

$$\mathcal{V}_{\text{opt}}(\omega) = \frac{1}{Z_i(\omega) + Z_i^*(\omega)} F_{\text{exc}}(\omega), \quad (9)$$

$$= \frac{1}{2R_r(\omega) + 2R_l} F_{\text{exc}}(\omega), \quad (10)$$

$$= H_{\text{opt}}(\omega) F_{\text{exc}}(\omega), \quad (11)$$

which defines the frequency response  $H_{\text{opt}}(\omega)$  for maximum power conversion. In this case, half of the average wave excitation power would be absorbed and the other half partly re-radiated and partly dissipated due to losses.

### 2.3 | Non-causality of real-time control system in time domain

Given (11), the optimal velocity can be written in the time domain as the convolution integral of the optimal transfer function and the excitation force:

$$\mathcal{v}_{\text{opt}}(t) = \int_{-\infty}^{\infty} h_{\text{opt}}(\tau) f_{\text{exc}}(t - \tau) d\tau. \quad (12)$$

One of the peculiarities of wave energy control is that the impulse response  $h_{\text{opt}}(t)$  becomes non-causal [20]: In order to compute the optimal velocity at time  $t$ , information about the excitation force is needed for both the period before and after  $t$ . The reason for this non-causality is the memory effect of wave radiation: The current hydrodynamic force due to self-motion of the device does not depend only on the current motion, but also on the previous motion. The resulting non-causality of the impulse response  $h_{\text{opt}}(t)$  leads to the need for future knowledge of the excitation force. This impulse response function is the inverse Fourier transform of the optimal transfer function and may be written as:

$$h_{\text{opt}}(t) = \frac{1}{2R_l} \delta(t) + k_{\text{opt}}(t), \quad (13)$$

$$k_{\text{opt}}(t) = \mathcal{F}^{-1} \left\{ H_{\text{opt}}(\omega) - \frac{1}{2R_l} \right\}, \quad (14)$$

where  $\delta(t)$  is the Dirac delta function. The inverse Fourier transform of  $H_{\text{opt}}(\omega)$  tends to a constant value as  $\omega \rightarrow \infty$ , thus the mathematical definition of  $k_{\text{opt}}(t)$  given above is required for the inverse Fourier transform to be well-defined. From the causality perspective,  $h_{\text{opt}}(t)$ , and  $k_{\text{opt}}(t)$  have the same characteristics as they only differ at time  $t = 0$  [4].

The *sub-optimal finite-horizon velocity* is introduced by truncating the convolution integral in (12), and it is defined as:

$$\mathcal{v}_{\text{opt}}^{T_b}(t) = \frac{1}{2R_l} f_{\text{exc}}(t) + \int_{-T_b}^{\infty} k_{\text{opt}}(\tau) f_{\text{exc}}(t - \tau) d\tau, \quad (15)$$

where the integral is truncated at the non-causal side ( $t < 0$ ) of the impulse response,  $k_{\text{opt}}(t)$ . This will be referred to as *single truncation*, while the term *double truncation* is used for the case where the integral is truncated at both sides to match the evenness of  $k_{\text{opt}}$ , i.e. when the integration limits are taken as  $[-T_b, +T_b]$ . It is further assumed that the excitation force is known accurately over the applied horizon, such that the sub-optimal velocity approaches the optimal velocity as the horizon becomes large;  $\mathcal{v}_{\text{opt}} = \lim_{T_b \rightarrow \infty} \mathcal{v}_{\text{opt}}^{T_b}$ .

The deviation of sub-optimal velocity from the optimal velocity, i.e. caused by this truncation, is expressed via goodness of fit (GoF):

$$\text{GoF}(T_b) = 1 - \sqrt{\frac{\Sigma(\mathcal{v}_{\text{opt}} - \mathcal{v}_{\text{opt}}^{T_b})^2}{\Sigma \mathcal{v}_{\text{opt}}^2}}. \quad (16)$$

### 2.4 | Useful power

The useful power is computed as the difference between absorbed power,  $P_a = P_e - P_r$ , and loss power  $P_l$ , [1]:

$$P_u = P_e - P_r - P_l, \quad (17)$$

where  $P_e$  is the excitation power and  $P_r$  is the radiation power. These power measures are derived in the time domain simply as follows:

$$P_e(t) = F_{\text{exc}}(t) \mathcal{v}(t), \quad (18)$$

$$P_r(t) = F_r(t) \mathcal{v}(t) = \mathcal{v}(t) \int_{-\infty}^{+\infty} r_r(\tau) \mathcal{v}(t - \tau) d\tau, \quad (19)$$

$$P_l(t) = F_l(t) \mathcal{v}(t) = R_l \mathcal{v}^2(t), \quad (20)$$

where  $F_r(t)$  and  $F_l(t)$  are the radiation and loss force, respectively, and  $r_r(t)$  is the impulse response of the radiation resistance  $R_r(\omega)$ .

Finally, the converted useful energy is the integration of  $P_u$  in time over the full length  $T_f$  of the time series,  $E_u = \int_0^{T_f} P_u dt$ , such that the average useful power is given by  $\bar{P}_u = E_u / T_f$ . The

maximum value for  $\bar{P}_u$  under the assumption of linearity, unconstrained motion and perfect knowledge of the future excitation force is well known [1, 2], and it can be computed directly as a combination of Equations (8) and (11):

$$\bar{P}_{u,\max}(\omega) = \frac{F_{\text{exc}}(\omega) F_{\text{exc}}(\omega)^*}{8 (R_r(\omega) + R_l)} \quad (21)$$

Denoting the idealised maximum useful power without losses ( $R_l = 0$ ) by  $P_u^i$ , the following relation may be straightforwardly derived:

$$\frac{\bar{P}_{u,\max}(\omega)}{P_u^i} = \frac{1}{1 + R_l/R_r(\omega)} \quad (22)$$

which equals to one in the case of zero loss damping,  $R_l = 0$ . It shows how the extractable power depends strongly on the loss damping.

### 3 | METHOD

#### 3.1 | Generic wave energy converter concepts

The following generic concepts for wave energy converter (WEC) are considered in this study:

- Floating sphere, oscillating in surge or heave
- Submerged sphere, oscillating in surge or heave
- A bottom-hinged flap, oscillating about a mean position of 0 or  $-30^\circ$ .

This makes a total of six configurations for single-mode oscillation, as illustrated in Figure 1, and with properties as listed in Table 1. The floating sphere has a draft equal to its radius and the submerged sphere has a distance of one diameter from its centre to the mean water level. The geometry of the bottom-hinged flap is adopted from [21] where a wide rectangular flap is located with 0.5 m gap from the seabed, while protruding 1.5 m above the mean free surface when upright. For the sake of simplification, the flap edges are here kept sharp-edged, and not rounded as they should be to reduce vortex shedding in a real device. Within the linearity assumption used in this study the results are not sensitive to how high the device reaches above the surface.

#### 3.2 | Hydrodynamic coefficients

The hydrodynamic coefficients (radiation resistance, added mass and excitation force coefficients) for generic concepts were computed by use of the potential flow solver WAMIT [22]. The geometry for the bottom-hinged flap was modelled in AeroHydro's MultiSurf software [23]. For all the geometries, the shape is defined with the high-order panel method. To mesh the geometry of the bottom-hinged flap in MultiSurf a total of

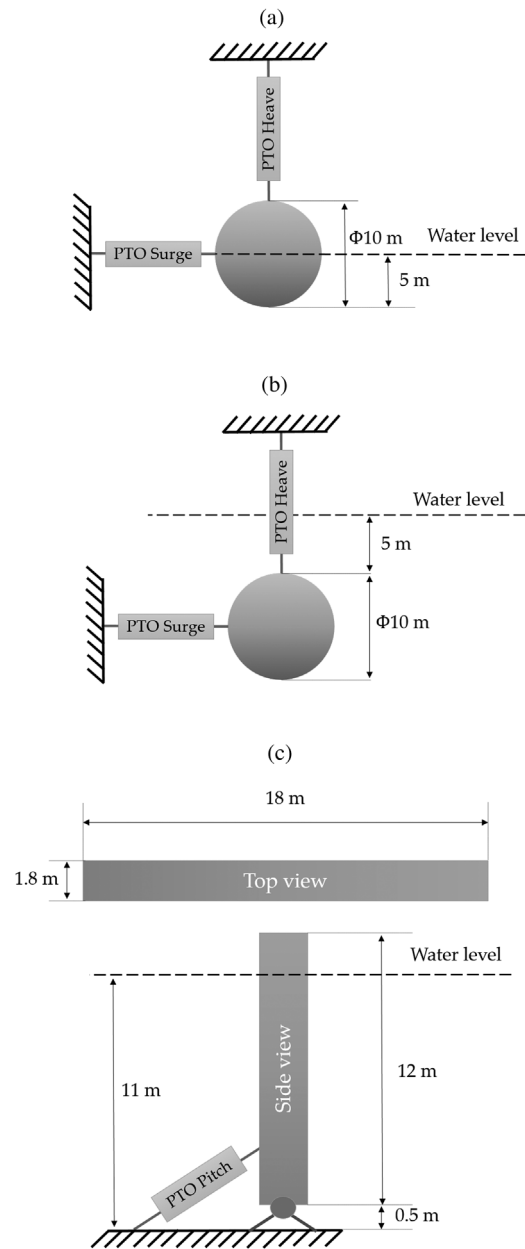


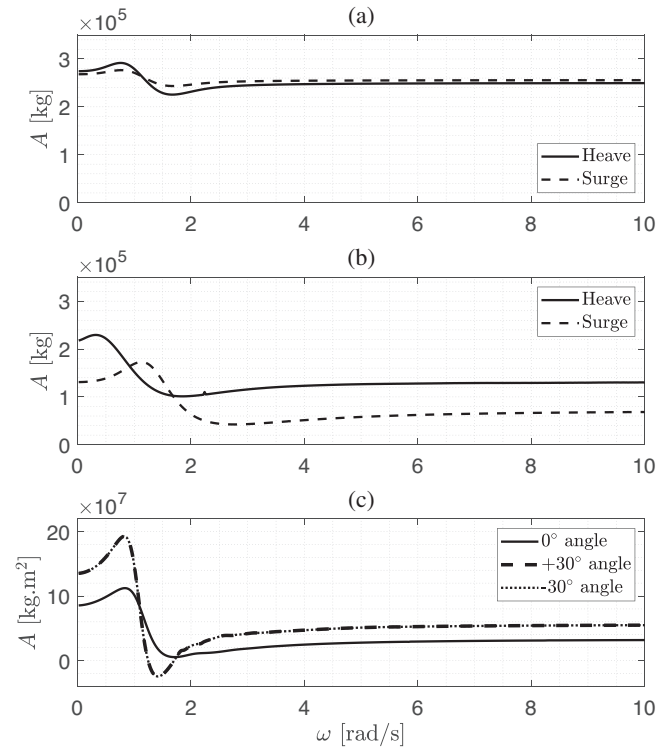
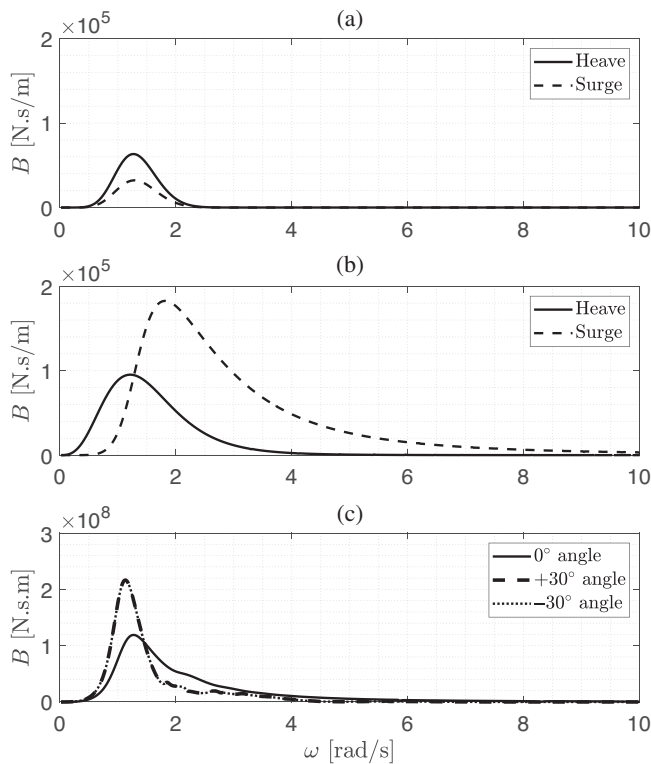
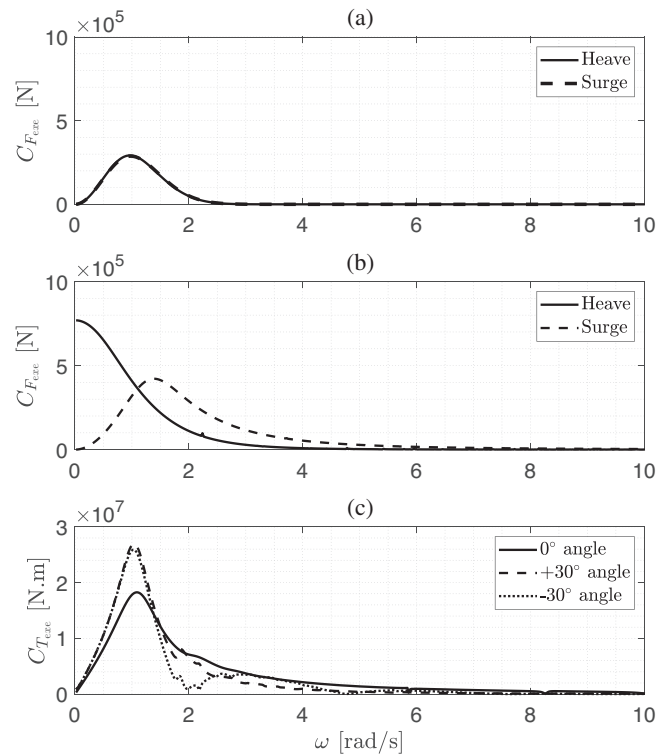
**FIGURE 1** Illustrations of the generic concepts studied. A notional power take-off (PTO) is included to indicate the power extraction in each mode of motion. (a) Floating sphere, surge or heave (two configurations). (b) Submerged sphere, surge or heave (two configurations). (c) Bottom-hinged flap, with mean position 0 or  $-30^\circ$  angle (two configurations)

59,835 panels were used. The floating and submerged spheres were defined analytically in WAMIT with a maximum panel length of 0.2 m.

For each generic concept, the radiation resistance, added mass and excitation force coefficient are depicted in Figures 2, 3 and 4, respectively. Note that the functionality for removal of irregular frequencies [22] has not been used, giving traces of singularities in some of the presented curves. The radiation damping and excitation force coefficients, are connected through reciprocity relations, cf. [1]. For the submerged sphere and the hinged flap, these hydrodynamic coefficients are some-

**TABLE 1** Properties of the generic concepts studied (see also Figure 1)

Parameter	Description	Value
<b>Floating sphere</b>		
$r$	Radius	5 m
$d$	Equilibrium draft	5 m
$b$	Water depth	Deep water
$\tau_{0,1}^{\text{float}}$	Time constant, surge	0.44 s
$\tau_{0,3}^{\text{float}}$	Time constant, heave	0.93 s
<b>Submerged sphere</b>		
$r$	Radius	5 m
$s$	Equilibrium submergence	5 m
$b$	Water depth	Deep water
$\tau_{0,1}^{\text{sub}}$	Time constant, surge	1.17 s
$\tau_{0,3}^{\text{sub}}$	Time constant, heave	1.17 s
<b>Bottom-hinged flap</b>		
$W \times L \times H$	Width $\times$ Thickness $\times$ Height	18 m $\times$ 1.8 m $\times$ 12 m
$z_b$	Vertical hinge position	-10.5 m
$b$	Water depth	11 m
$\theta_0$	Equilibrium angle	0 and $-30^\circ$
$\tau_{0,0^\circ}$	Time constant, upright	0.58 s
$\tau_{0,30^\circ}$	Time constant, inclined	0.77 s

**FIGURE 3** Added mass for all geometries and modes of motion. (a) Submerged sphere. (b) Floating sphere. (c) Bottom-hinged flap**FIGURE 2** Radiation resistance for all geometries and modes of motion. (a) Submerged sphere. (b) Floating sphere. (c) Bottom-hinged flap**FIGURE 4** Excitation force and torque coefficient for all geometries and modes of motion. (a) Submerged sphere. (b) Floating sphere. (c) Bottom-hinged flap

what similar in terms of frequency range. The floating sphere differs from the two other concepts, where both excitation and radiation for the surge mode are shifted towards higher frequencies, and for the heave mode towards lower frequencies. Note also that the floating sphere in heave mode is the only concept that retains excitation as the frequency approaches zero, and that the inclined flap has larger radiation and excitation than the upright flap.

### 3.3 | Waves and excitation

In this study, to compute the excitation force and torque, the JONSWAP spectrum [25] is assumed for the wave elevation:

$$S_J(\omega) = A_\gamma S_{PM}(\omega) \gamma^{\exp\left(-0.5\left(\frac{\omega-\omega_p}{\sigma\omega_p}\right)^2\right)}, \quad (23)$$

where  $\gamma$  is a non-dimensional peak shape parameter, and  $\sigma$  is the spectral width parameter ( $\sigma = \sigma_a = 0.07$  for  $\omega \leq \omega_p$ ,  $\sigma = \sigma_b = 0.09$  for  $\omega > \omega_p$ ),  $A_\gamma = 1 - 0.287 \ln(\gamma)$  is a normalizing factor and  $S_{PM}$  is the Pierson–Moskowitz (PM) spectrum given by

$$S_{PM}(\omega) = \frac{5}{16} H_s^2 \omega_p^4 \omega^5 \exp\left(-\frac{5}{4} \frac{\omega}{\omega_p}\right). \quad (24)$$

Here,  $H_s$  is the significant wave height and  $\omega_p$  is the peak angular frequency of the spectrum.

The excitation force (or correspondingly, excitation torque) is now computed as a superposition of frequency components  $\omega_i$  according to

$$F_{exc}(t) = \sum_i a_i \cos(\omega_i t + \angle f(\omega_i) + \phi_{i,rand}), \quad (25)$$

$$a_i = |f_{exc}(\omega_i)| \sqrt{2S_J(\omega_i) d\omega}, \quad (26)$$

where  $f_{exc}(\omega_i)$  is the complex excitation force coefficient, and  $a_i$  is the amplitude corresponding to each component of the excitation spectrum  $S_{exc}(\omega_i) = |f_{exc}(\omega_i)|^2 S_J(\omega_i)$ . The phase is randomised through the parameters  $\phi_{i,rand}$  which is evenly distributed over  $]0, 2\pi[$ .

The study is focused on sea states with energy periods of 6.5, 9.5 and 12.5 s which represent the lower, middle and upper range for typical wave climates relevant for wave energy utilisation in general, whereas the full data set includes energy periods ranging from 3.5 to 15.5 s with steps of 0.5 s. Wave climate information for various coastal sites around the world can be found in [24–27]. The JONSWAP shape factor,  $\gamma$ , was considered 3.3 while in the full data set, it varied between 1.0 and 5.0 in steps of 0.1. The significant wave height of 2.5 m was used throughout, except when amplitude constraints were considered, where the range 0.5–12.5 m was considered.

A time series duration  $T_f$  of 30 min is used for the computation of GoF and average useful power.

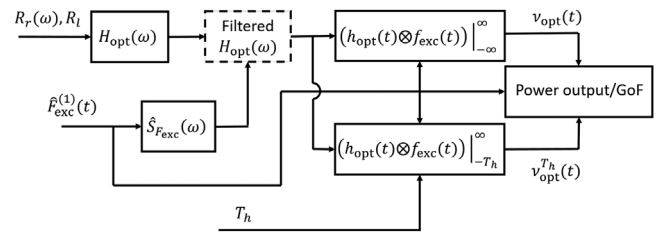


**FIGURE 5** Information flow in the computation of goodness of fit (GoF) and power output as function of prediction horizon  $T_b$ . (1) The estimated excitation force,  $\hat{F}_{exc}(t)$ , and the corresponding spectrum,  $\hat{S}_{exc}(\omega)$ , is here assumed to be known. In reality, it has to be computed by Kalman filtering or other methods e.g. (see [18, 28–33]), and the optional filtering has to be done carefully not to distort the phase of the signal

### 3.4 | Main variables: Prediction horizon and loss coefficient

The course of the computation is depicted in Figure 5, which shows where the prediction horizon length  $T_b$  and loss coefficient  $R_l$  enter the problem to compute the GoF and average useful power, which are the main outputs considered.

The length  $T_b$  of the prediction horizon is varied from 0.0 to 15 s, which is found sufficient to reveal the characteristics of the studied generic concepts. The optimal power is achieved for the infinite prediction horizon which here is approximated as the maximum available time of the impulse response function,  $k_{opt}(t)$ . Choosing the range of loss damping is somewhat more difficult. As the details of the conversion machinery is not considered in this study, an educated guess has to be applied for the losses involved. The applied range of losses has been chosen based on considerations of expected hydrodynamic drag, which when linearised sets a limit for the minimum expected total loss. Following this approach, the range for  $R_l$  has been selected as [5, 100] kNs/m in all oscillation modes for the floating and submerged sphere, and as [2, 100] MNms for the hinged flap. To put this in context, for the floating sphere in heave and the bottom-hinged upright flap the lower bounds are found to give an average efficiency  $\eta = \bar{P}_u / (\bar{P}_u + \bar{P}_l)$  of about 0.9 in the sea state with significant wave height  $H_s = 2.5$  m and energy period  $T_e = 9.5$  s.

The frequency response of the optimal transfer function (11) and the impulse response function are plotted in Figures 6 and 7, respectively, for all generic concepts. An optional filtering is applied in order to reduce the prediction requirements and non-causality of the optimal velocity, cf. [4, 18]. The filtering is done by excluding the frequency range where the excitation spectrum is below a certain threshold, as further explained in Subsection 3.5.

The optimal impulse response function is also illustrated for different loss damping in Figure 8 which shows that increasing the losses decreases the value at  $t = 0$  and gives faster decay with distance from zero time.

### 3.5 | Other variations

In addition to what is described above, the following considerations have been made:

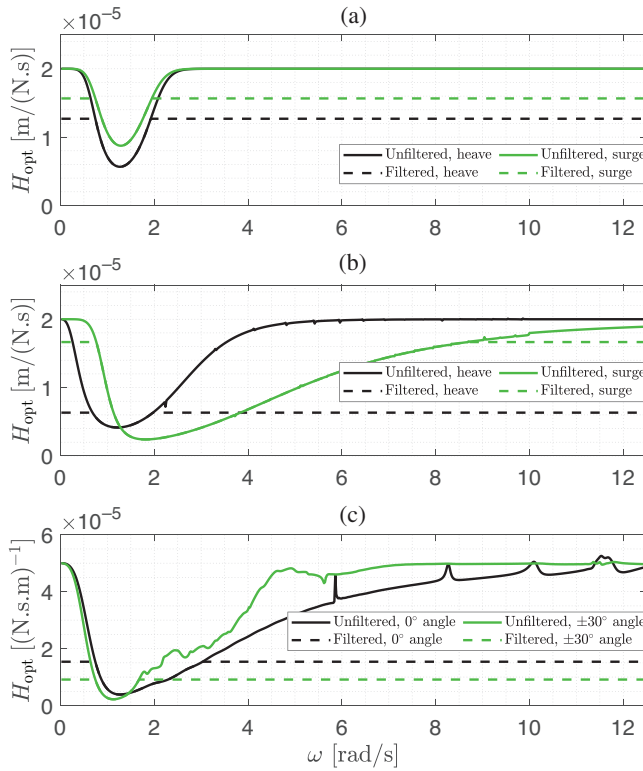


**FIGURE 6** Frequency response  $H_{\text{opt}}(\omega)$  of the optimal transfer function between the excitation force and optimal velocity for all generic concepts and damping value  $R_f = 25$  kNs/m, and  $R_\theta = 10$  MNms for submerged and floating sphere and bottom-hinged flap, respectively. Also shown is the filtered transfer function based on the excitation spectrum for  $T_e = 6.5$  s and filtering limit set to 5%. The spikes seen in some of the curves are due to singularities in the numerical solution of hydrodynamic coefficients, cf. Section 3.2. (a) Submerged sphere. (b) Floating sphere. (c) Bottom-hinged flap

- As reference, the no-prediction useful power is computed considering a constant transfer function for each generic concept. The radiation resistance in  $H_{\text{opt}}(\omega)$  is considered constant and is equal to the radiation resistance value for which the no-prediction power is maximum: With a given sea state, the frequency argument of  $H_{\text{opt}}(\omega)$  is varied, computing the average useful power for each frequency value, and the no-prediction transfer constant is identified as the one giving the best result. Note that the chosen constant will vary between sea states, and it does not necessarily correspond to the value where the frequency response  $H_{\text{opt}}(\omega)$  has its minimum, i.e. where the radiation resistance  $R_r(\omega)$  is maximum.
- The sensitivity to prediction accuracy is studied assuming a noise spectrum similar to the wave spectrum, and defining the noise ratio as the ratio of the standard deviations,  $\sigma_n/\sigma_F$ , ranging from 0.0 to 1.0 with steps of 0.05. The significant wave height for the noise spectrum is taken as  $H_{s,n} = 4\sigma_n$ , while other parameters such as shape factor and energy period are considered as before, i.e. explained in Subsection 3.3. The generated noise signal in time domain is then added to the excitation force to compute the useful power. Figure 9 compares the excitation force with different noise

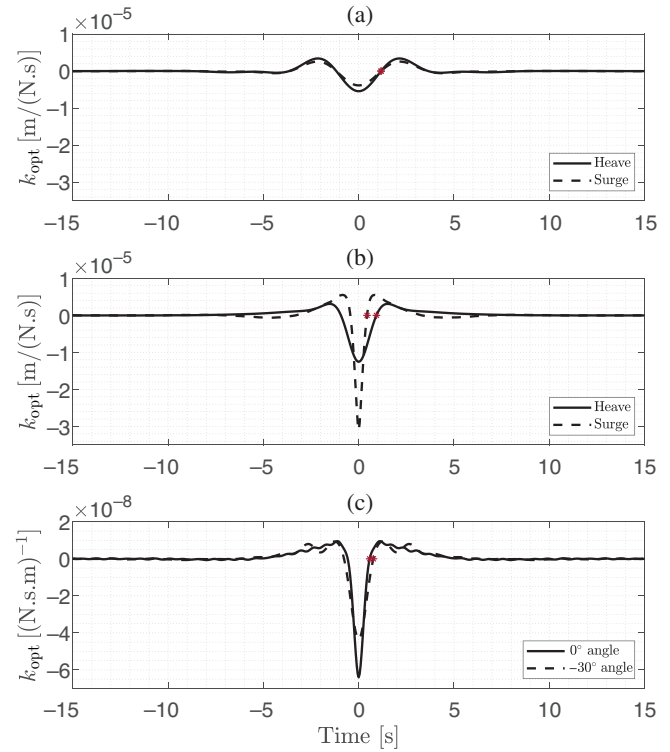


**FIGURE 7** Impulse response of the transfer function,  $k_{\text{opt}}(t)$ , for all geometries in the case of loss damping  $R_f = 25$  kNs/m for the submerged and floating spheres, and  $R_\theta = 10$  MNms for bottom-hinged flap. Red markers show the first zero crossing. (a) Submerged sphere. (b) Floating sphere. (c) Bottom-hinged flap

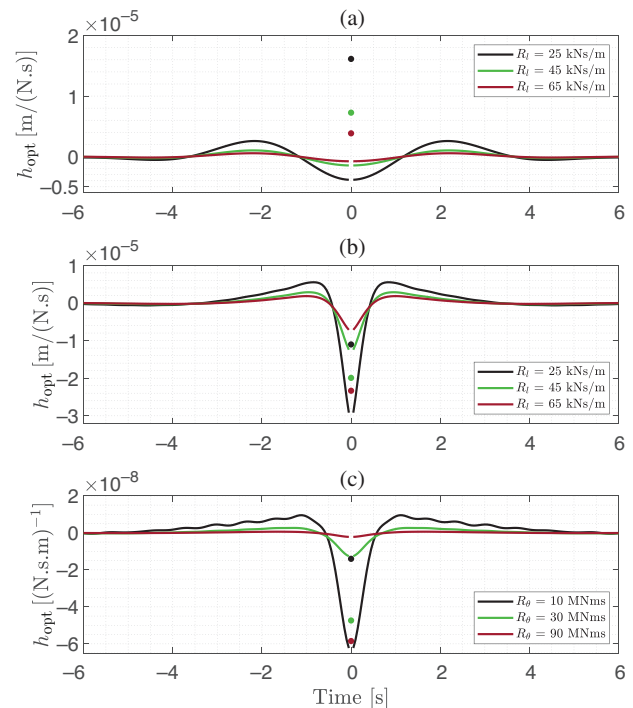


**FIGURE 8** Impulse response of the transfer function,  $h_{\text{opt}}(t)$ , for the surging sphere and the upright bottom-hinged flap, shown for different loss damping coefficients. (a) Submerged sphere, surge. (b) Floating sphere, surge. (c) Bottom-hinged flap,  $0^\circ$  flap angle



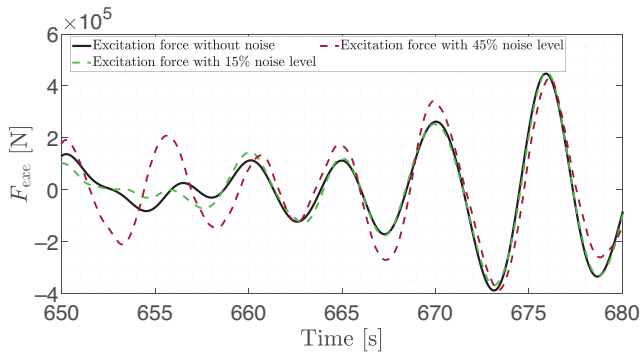


**FIGURE 9** The excitation force without noise, and with different noise levels for submerged sphere in surge mode and energy period  $T_e = 6.5$  s

levels, for submerged sphere in surge mode and energy period  $T_e = 6.5$  s.

- The effect of oscillation amplitude constraints is studied in a simplified, sub-optimal manner by setting the velocity signal to zero at intervals where the position response exceeds the amplitude constraints,

$$\mathbf{v}_{\text{constr}}^{T_b}(t) = \begin{cases} \mathbf{v}_{\text{opt}}^{T_b}(t) & |\eta_{\text{opt}}^{T_b}(t)| \leq \eta_{\text{max}}, \\ 0 & \text{otherwise} \end{cases} \quad (27)$$

where  $\eta_{\text{opt}}^{T_b}(t) = \int_0^t \mathbf{v}_{\text{opt}}^{T_b}(t) dt$ . This would provide a response that resembles what an infinitely strong and rapid optimally controlled machinery would give. It means the manipulated velocity response is close to, but not equal to the constrained optimal solution. Although interesting, it is not in the scope of this paper to compare this constrained solution to the constrained optimal velocity profile. When applied, the amplitude constraints are set to  $\pm 3$  m for the floating and submerged sphere concepts and to  $\pm 15^\circ$  for the hinged flap.

- Finally, the sensitivity of the prediction requirement to filtering of the transfer function is studied. The cut-off frequency of the optimal transfer function is chosen by cutting the excitation spectrum at a percentage of the peak value, i.e. called the filtering limit. The filtering limit is varied over [5, 50]% to evaluate its effect on power output versus prediction horizon length. This gives an upper and a lower filter frequency. The filtered version of the optimal transfer function is then defined by truncation at the largest function value between the two filter frequencies as shown in Figure 6.

### 3.6 | Normalization

To make the analysis more general, and comparable between concepts, the prediction horizon and damping, as well as the useful power are normalised. The prediction horizon is normalised by the first zero crossing of the impulse response function  $k_{\text{opt}}(t)$ , see Figure 7, as  $N_T = T_b/\tau_0$ . The damping is normalised by the value of radiation resistance at the energy period of the sea state,  $N_R = R_l/R_r(\omega_e) = R_l/R_r(2\pi/T_e)$ . Finally, for

each generic concept, the sub-optimal power is normalised with the optimal power for the sea state in question,  $N_P = \bar{P}_u/P_u^{\text{opt}}$ , where  $P_u^{\text{opt}}$  is computed as the limit  $\bar{P}_u$  for large prediction horizon,  $P_u^{\text{opt}} = \lim_{T_b \rightarrow \infty} \bar{P}_u$ . The term ‘relative’ refers to this normalization of the parameters throughout the paper.

The size of the oscillating bodies has been kept constant in this study. Varying the size could be seen as equivalent to varying the sea state parameters, and could thus have been incorporated by making both sea states and hydrodynamic parameters non-dimensional. We have chosen, however, to keep these quantities dimensional to ease interpretation of results for body sizes and sea states we consider to be representative of realistic cases.

## 4 | RESULTS

The input parameters used for the different sensitivity studies carried out to investigate the prediction requirement are given in Table 2, and the results for each parameter variation are presented below.

### 4.1 | GoF for single and double truncation

For all concepts, Figure 10 displays the GoF with single and double truncation of the integral in the computation of the optimal trajectory, i.e. Equation (15) with integration limits  $[-Th, \infty]$  and  $[-Th, +Th]$ , respectively. Double truncation is found to give inferior GoF compared to single truncation for all generic concepts. The same is true for the average useful power. For the remaining analysis in this paper, therefore, only single-truncated results will be presented. Although the GoF results carry over to useful power, the useful power has been used as the main output throughout the study.

### 4.2 | Sensitivity to loss damping

Results for maximum average useful power versus relative damping,  $r_d = R_l/R_r(\omega_e)$ , are shown in Figure 11, which also include results for the no-prediction case. Note that these maximum power results for irregular waves, which are found as the asymptotic value for increasing prediction horizon, follow the same trend as given by the theoretical relation (22) for maximum useful power versus dissipative loss in a regular wave.

**When the dissipative loss is high, there is no benefit in predicting the incoming waves:** The tail for increasing damping in all curves shows perfect alignment between no-prediction case and the optimal useful power. Note that this may not be true when constraints are included. Note also that, provided our guess for damping levels gives comparability across concepts, the no-prediction case converges slower to the optimal solution for the hinged flap than for the floating and submerged sphere concepts.

With results established for the maximum useful power under optimal non-causal control, we may compute the

TABLE 2 Summary of parameter studies

Parameter	Concept	Range	Sea state			
			$H_s$	$T_e$	$\gamma$	Loss damping
Loss damping	Floating and submerged sphere	[5, 100] kNs/m	2.5 m	6.5, 9.5, 12.5 s	3.3	–
	Bottom-hinged flap	[2, 100] MNsm				
JONSWAP shape factor	Floating and submerged sphere	[1, 5] s with steps of 0.1 s				–
	Bottom-hinged flap					10 MNsm
Energy period	Floating and submerged sphere	[3.5, 15.5] s with steps of 0.5 m		–	3.3	25 kNs/m
	Bottom-hinged flap					10 MNsm
Noise	Floating and submerged sphere	5, 15, 30, 45%		6.5, 9.5, 12.5 s		25, 45, 65 kNs/m
	Bottom-hinged flap					10, 30, 90 MNsm
Constraint	Floating and submerged sphere	$\pm 3$ m	[0.5, 12.5] m with steps of 0.5 m			25 kNs/m
	Bottom-hinged flap	$\pm 15^\circ$				10 MNsm
Filtering	Floating and submerged sphere	5, 10, 20, 30, 40, 50%	2.5			25 kNs/m
	Bottom-hinged flap					10 MNsm

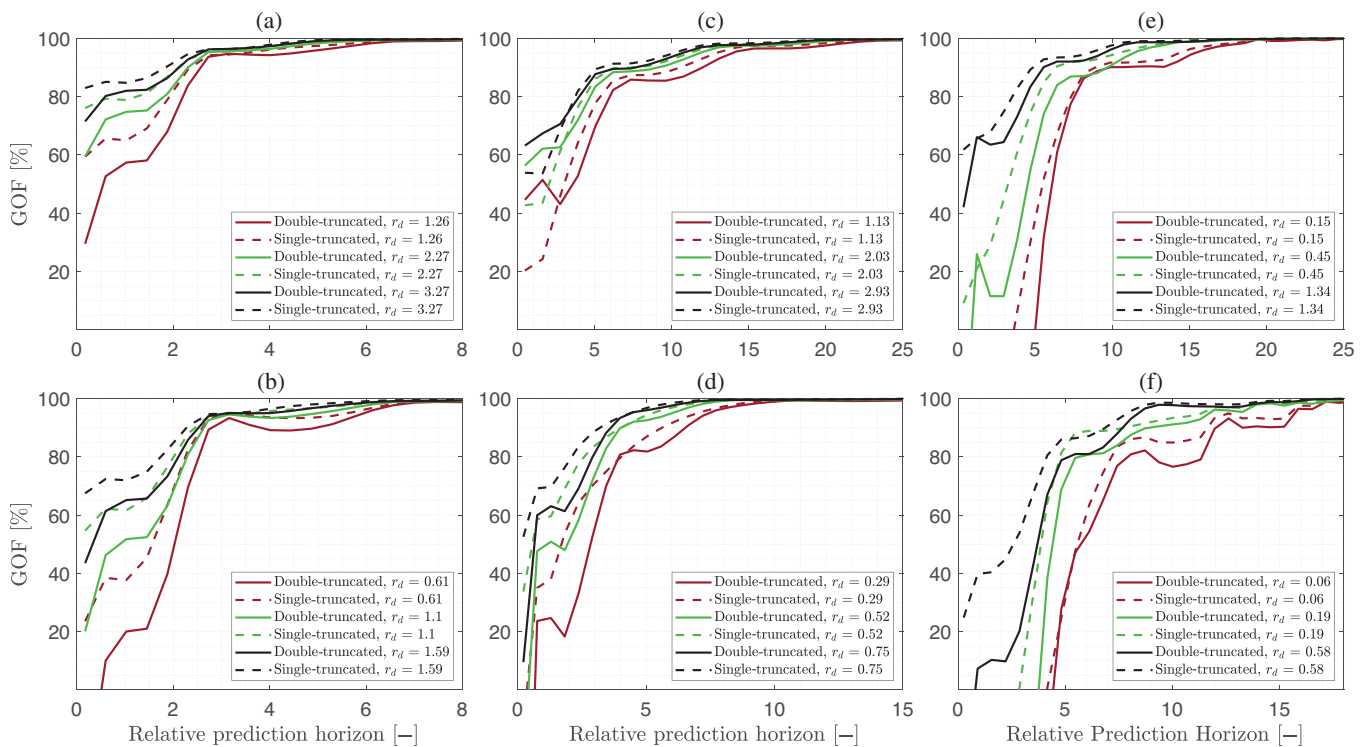
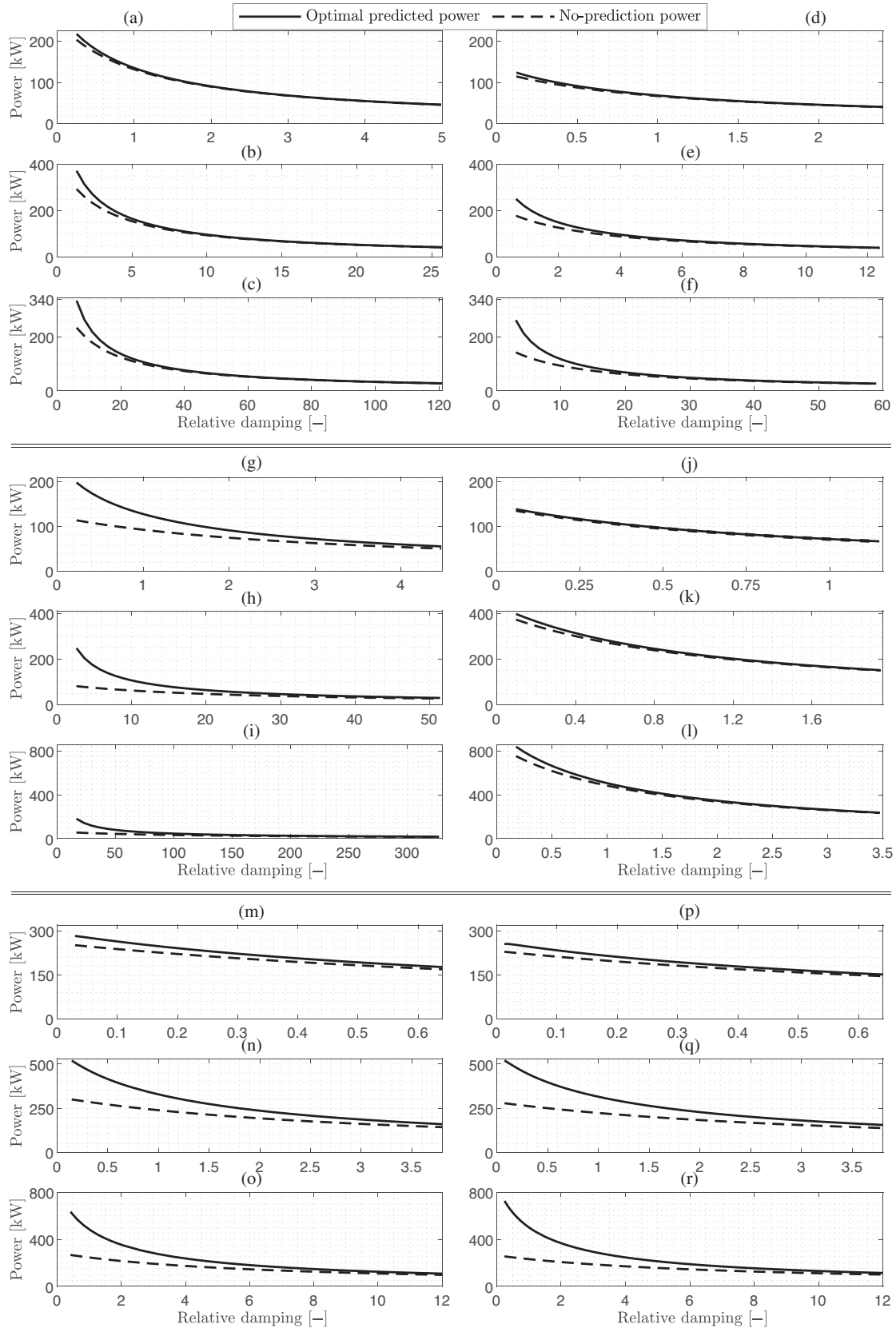


FIGURE 10 Goodness of fit for double and single-truncated data for  $T_e = 6.5$  s, where relative damping is defined as  $r_d = R_l/R_r(\omega_e)$ . (a, b) Submerged sphere in surge and heave motion, respectively. (c, d) Floating sphere in surge and heave motion, respectively. (e, f) Bottom-hinged flap with zero and  $-30^\circ$  pitch angle, respectively

non-dimensional useful power and look at the influence of limiting the prediction horizon. Figure 12 shows the contours of relative power for different values of relative prediction horizon and relative damping for all generic concepts. In general, the useful power is strongly reduced for short prediction horizon

and low loss damping. As the loss damping increases, a shorter prediction horizon is required to approach the maximum power absorption. This should be expected; when the damping in the system goes from being dominated by the radiation resistance to being dominated by the loss damping the importance of the



**FIGURE 11** Maximum average power with ideal prediction and no-prediction versus different damping level for all concepts, where relative damping is defined as  $r_d = R_i/R_e(\omega_e)$ . (a, b, c) Submerged sphere in surge motion for  $T_e = 6.5$  s,  $T_e = 9.5$  s and  $T_e = 12.5$  s, respectively. (d, e, f) Submerged sphere in heave motion for  $T_e = 6.5$  s,  $T_e = 9.5$  s and  $T_e = 12.5$  s, respectively. (g, h, i) Floating sphere in surge motion for  $T_e = 6.5$  s,  $T_e = 9.5$  s and  $T_e = 12.5$  s, respectively. (j, k, l) Floating sphere in heave motion for  $T_e = 6.5$  s,  $T_e = 9.5$  s and  $T_e = 12.5$  s, respectively. (m, n, o) Bottom-hinged flap with zero pitch angle for  $T_e = 6.5$  s,  $T_e = 9.5$  s and  $T_e = 12.5$  s, respectively. (p, q, r) Bottom-hinged flap with  $-30^\circ$  pitch angle for  $T_e = 6.5$  s,  $T_e = 9.5$  s and  $T_e = 12.5$  s, respectively

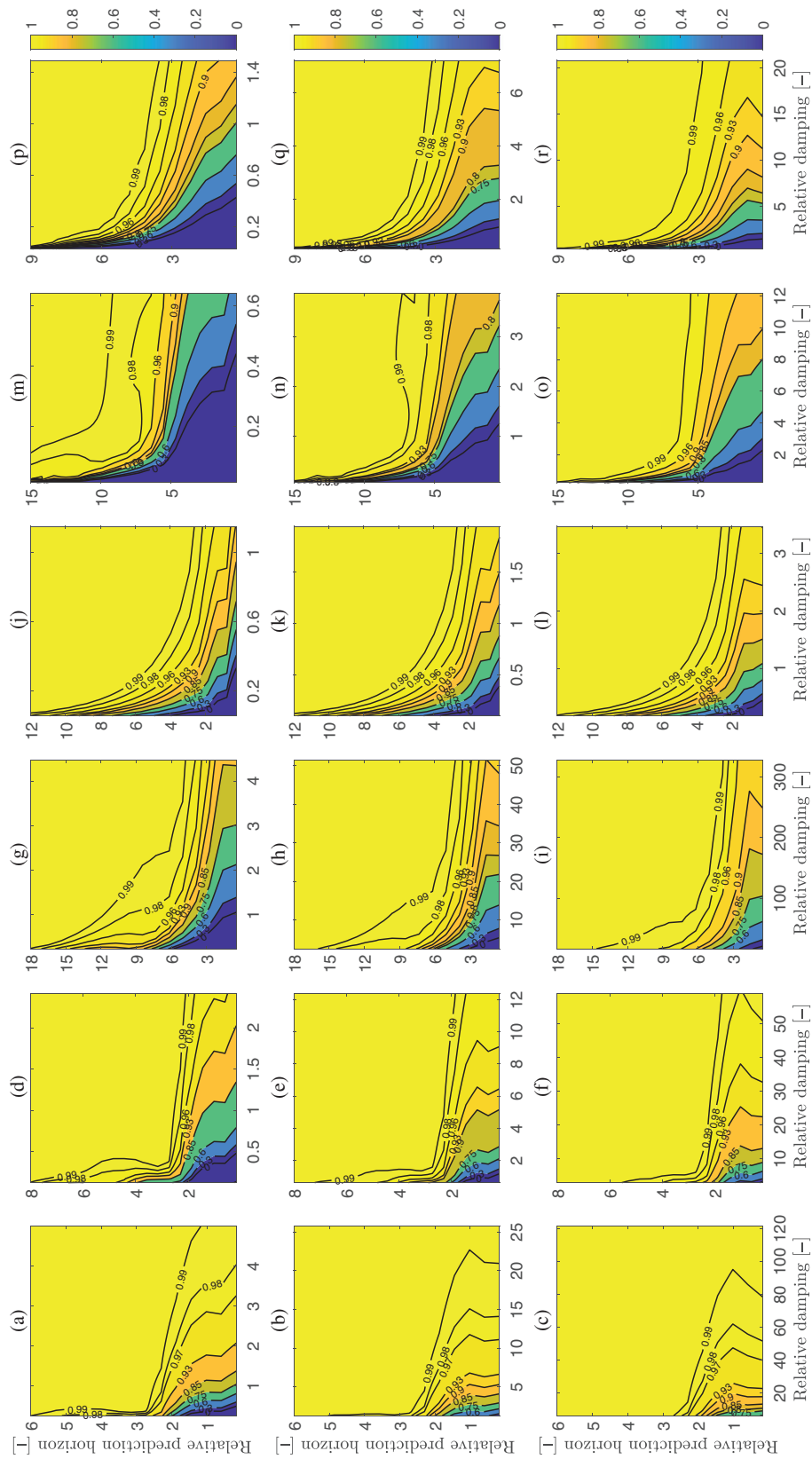


**FIGURE 12** Relative power for different prediction horizon and damping for all concepts, where relative damping is defined as  $r_d = R_l/R_r(\omega_e)$ . (a, b, c) Submerged sphere in surge motion for  $T_e = 6.5$  s,  $T_e = 9.5$  s and  $T_e = 12.5$  s, respectively. (d, e, f) Submerged sphere in heave motion for  $T_e = 6.5$  s,  $T_e = 9.5$  s and  $T_e = 12.5$  s, respectively. (g, h, i) Floating sphere in surge motion for  $T_e = 6.5$  s,  $T_e = 9.5$  s and  $T_e = 12.5$  s, respectively. (j, k, l) Floating sphere in heave motion for  $T_e = 6.5$  s,  $T_e = 9.5$  s and  $T_e = 12.5$  s, respectively. (m, n, o) Bottom-hinged flap with zero pitch angle for  $T_e = 6.5$  s,  $T_e = 9.5$  s and  $T_e = 12.5$  s, respectively. (p, q, r) Bottom-hinged flap with  $-30^\circ$  pitch angle for  $T_e = 6.5$  s,  $T_e = 9.5$  s and  $T_e = 12.5$  s, respectively



memory effect in wave radiation reduces. The optimal control problem goes from being non-causal with strong dependence on prediction of future excitation, to being predominantly causal. This transformation to causality can also be understood from Figure 8 where the content of the optimal impulse response function for most configurations becomes dominated by the value at  $t = 0$  for high losses.

Furthermore, Figure 13 shows that for all generic concepts, except the floating sphere in surge mode, the sea state with energy period  $T_e = 6.5$  s has very small difference between the optimally controlled case and the no-prediction case. As  $T_e$  increases, the no-prediction average power diverges from the optimal control result especially when the loss damping is low. The exception is the floating sphere in heave mode, where unlike other concepts, the no-prediction control continues to give fairly good performance also when the wave period increases. This behaviour is related to the value of the frequency response (11) around dominant frequencies of the sea state. Looking back at Figure 6, it may be observed that for the floating sphere in heave mode, the wave frequency,  $\omega_e$ , is located within the pass-band frequency of the optimal transfer function and close to the peak of the excitation force coefficient unlike other concepts, at angular frequencies  $2\pi/9.5$  s = 0.66 rad/s and  $2\pi/12.5$  s = 0.50 rad/s.

### 4.3 | Sensitivity to the JONSWAP spectrum shape factor

The effect of the shape factor,  $\gamma$ , for the JONSWAP wave spectrum has been investigated, and it was found that varying the shape factor in the range [1,5] does not significantly change the required prediction horizon for any of the generic concepts (see the Appendix).

### 4.4 | Sensitivity to energy period

Sensitivity of the prediction requirement to the energy period,  $T_e$ , is demonstrated in Figure 14. All contour plots of the  $T_e$ -sensitivity show a region of lower relative power for small  $T_e$  and short prediction horizon. The position of this region relates to the 'stop-band' of the optimal transfer functions in each case, i.e. the frequency range where the radiation resistance is comparable to or larger than the loss damping. In that range, the radiation force has a governing impact on the system dynamics, and the prediction has relatively stronger importance.

It is also worth noting that for all concepts except the floating sphere in heave motion, the optimal power versus energy period has a maximum within the  $T_e$  range [5.5, 13.5] s. For an ideal unconstrained system, these curves would ascend monotonously for increasing wave period. The reason why they become limited is the dissipative losses: As the relative damping  $R_i/R_r(\omega_e)$  increases due to the reducing trend of  $R_r(\omega_e)$  when the wave period increases, the maximum power output follows the descending trend seen in Figure 11, and (22) instead of stay-

ing at the very left of these curves. With zero loss, the decline in excitation coefficients when the wave period increases can be compensated by an increase in the motion response to produce the outgoing waves needed for optimal interference with incoming waves. When the loss damping gradually becomes more and more dominant, this does not work anymore, and the result is that the optimal velocity and thereby the maximum power limits itself.

The floating sphere in heave motion has an excitation magnitude that approaches its maximum at the limit of long wave periods, and also correspondingly has a weaker decline of the radiation resistance than the other concepts considered. It will, however, also eventually see the same decline in power output versus energy period as other concepts, but for much higher wave periods.

### 4.5 | Sensitivity to noise

The effect of a noisy prediction is investigated in Figure 15 where the power output both with long horizon and with no-prediction diminishes with increasing noise level. The relative power reduces with a similar rate for different loss damping, and the negative effect of the noise level on the optimal predicted power is similar in different sea states. Note that the normalization here is based on the optimal predicted power with no noise. The prediction horizon required to achieve close-to-optimal power has not changed with the noise level as can be seen in Figure 16. In other words, although the curves of relative power converge to lower optimal power as the noise increases, the prediction horizon required to almost obtain this optimal power remains fairly constant for different noise levels.

### 4.6 | Sensitivity to constraints

The effect of introducing amplitude constraints is shown in Figure 17, where the amplitude has been limited to  $\pm 3$  m for the floating and submerged sphere and  $\pm 15^\circ$  for the bottom-hinged flap. Note that the results have been normalised with the unconstrained optimal power. It may be observed that as the wave height increases and the constraints engage, the prediction horizon has less influence. Moreover, as should be expected, the relative power decreases monotonically with increasing wave height after the constraints kick in. Comparing different sea states for the same generic concept shows that constraints start to engage at smaller  $H_s$  as the energy period is increased. This implies that the amplitude of the WEC oscillation becomes larger at sea states with higher  $T_e$ . This might not be immediately intuitive from looking at the peak value of the excitation spectrum which reduces for all concepts as wave period increases, except floating sphere in heave motion. For these concepts, this reduction in excitation is however more than compensated by the increase in the optimal transfer function for large wave periods (Figure 6) as it is the product of these two that govern the amplitude response.

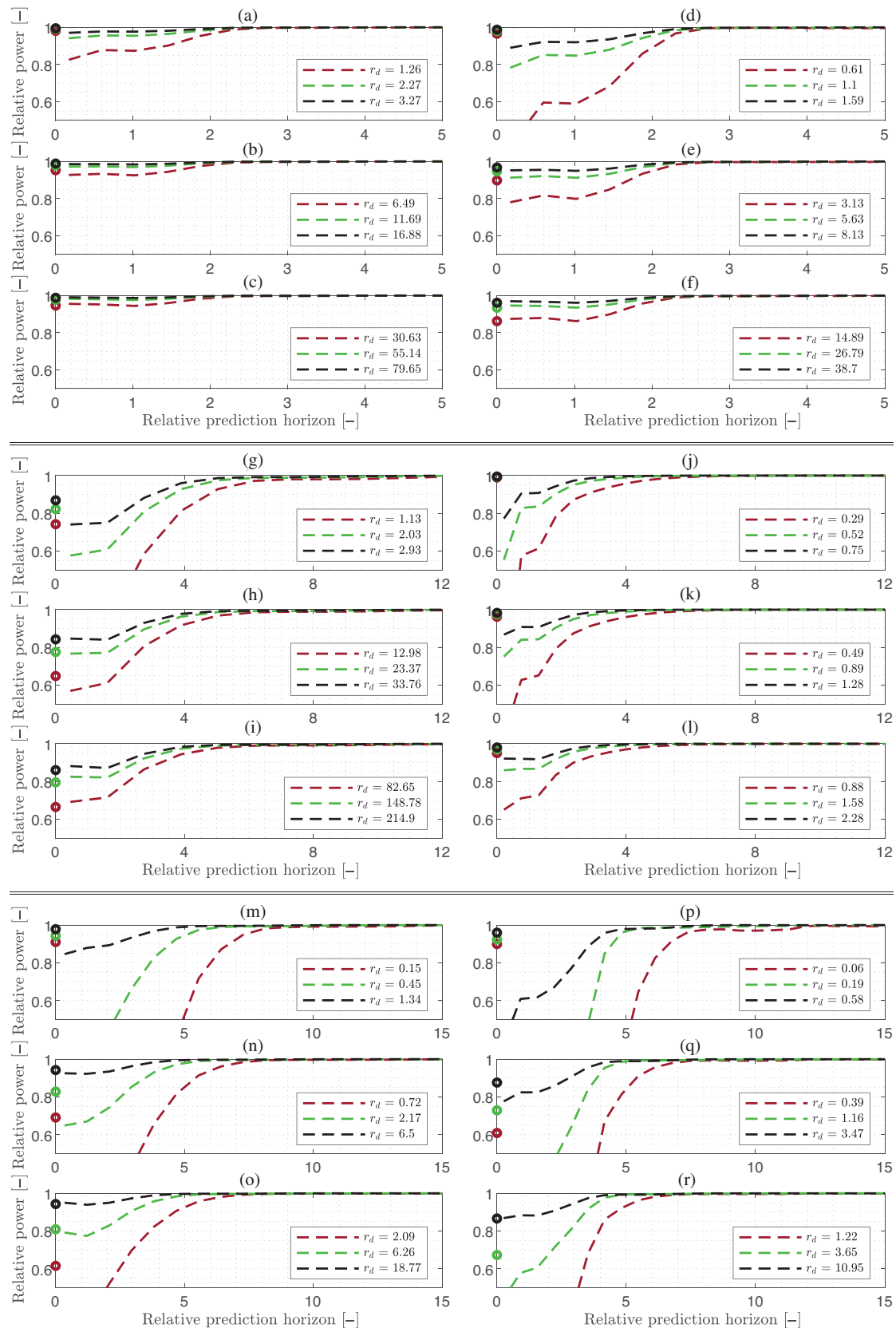


**FIGURE 13** Relative power for different prediction horizon and three different relative damping,  $r_d = R_l / R_r(\omega_e)$ , for all concepts. Circles show the no-prediction power corresponding to each relative damping. (a, b, c) Submerged sphere in surge motion for  $T_e = 6.5$  s,  $T_e = 9.5$  s and  $T_e = 12.5$  s, respectively. (d, e, f) Submerged sphere in heave motion for  $T_e = 6.5$  s,  $T_e = 9.5$  s and  $T_e = 12.5$  s, respectively. (g, h, i) Floating sphere in surge motion for  $T_e = 6.5$  s,  $T_e = 9.5$  s and  $T_e = 12.5$  s, respectively. (j, k, l) Floating sphere in heave motion for  $T_e = 6.5$  s,  $T_e = 9.5$  s and  $T_e = 12.5$  s, respectively. (m, n, o) Bottom-hinged flap with zero pitch angle for  $T_e = 6.5$  s,  $T_e = 9.5$  s and  $T_e = 12.5$  s, respectively. (p, q, r) Bottom-hinged flap with  $-30^\circ$  pitch angle for  $T_e = 6.5$  s,  $T_e = 9.5$  s and  $T_e = 12.5$  s, respectively

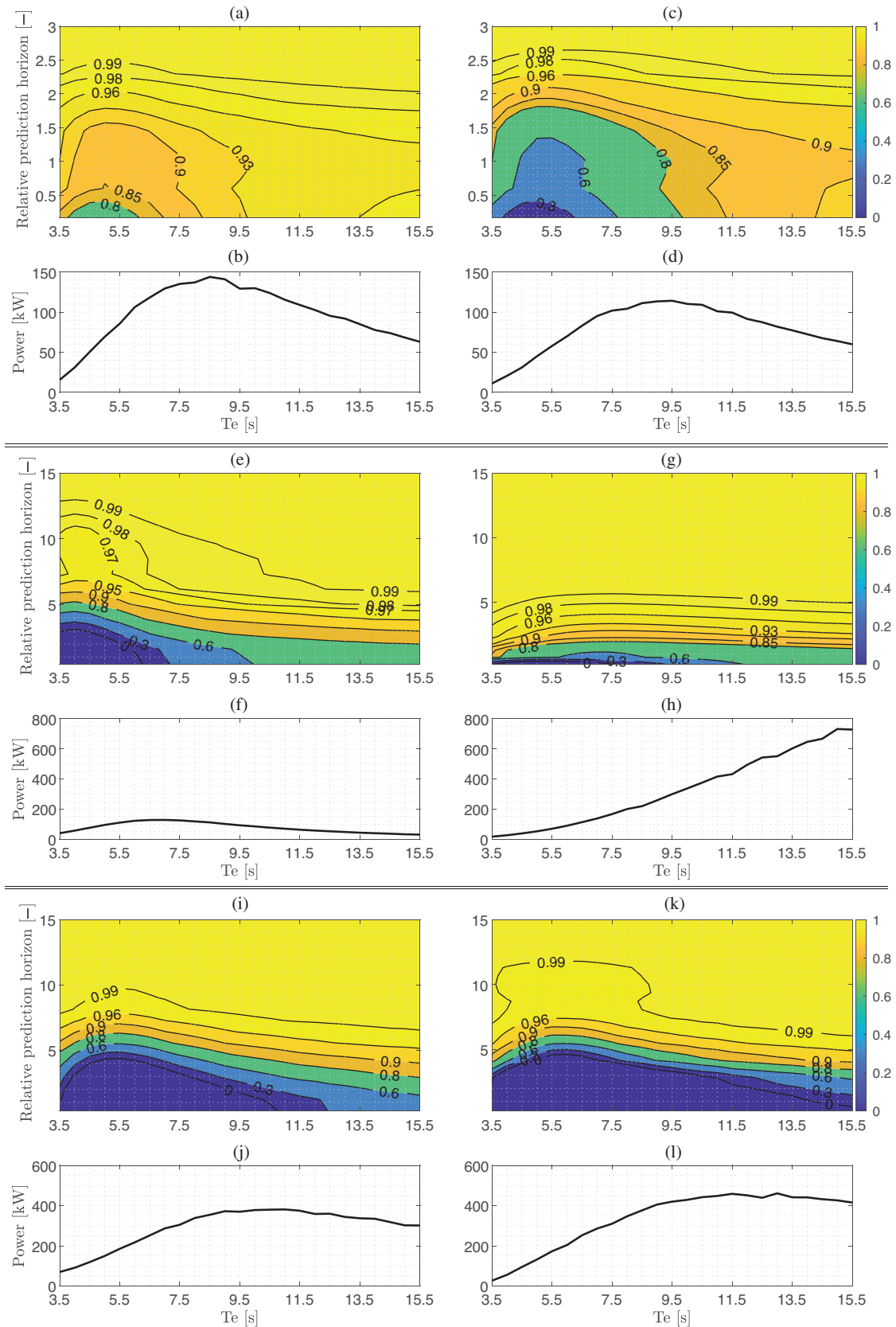


**FIGURE 14** Sensitivity of useful power to length of prediction horizon and energy period for all concepts. Below each contour plot of relative power a curve shows the optimal power for each concept. (a, b) Submerged sphere in surge motion, for damping of 25 kNs/m. (c, d) Submerged sphere in heave motion, for damping of 25 kNs/m. (e, f) Floating sphere in surge motion, for damping of 25 kNs/m. (g, h) Floating sphere in heave motion, for damping of 25 kNs/m. (i, j) Bottom-hinged flap with zero mean pitch angle, for damping of 10 MNsm. (k, l) Bottom-hinged flap with mean angle of  $-30^\circ$ , for damping of 10 MNsm

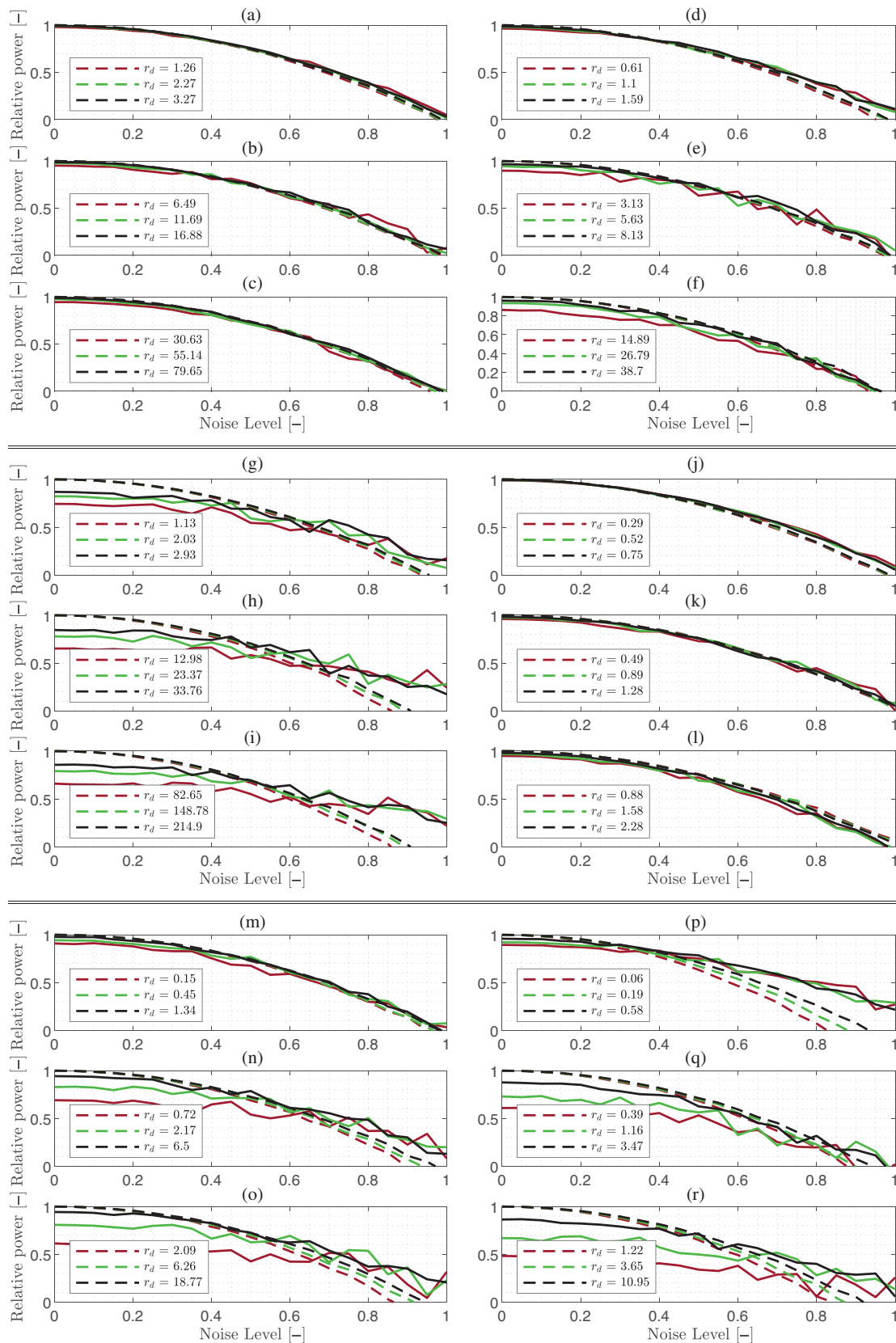


**FIGURE 15** Relative power versus noise level for all concepts. Solid lines show the no-prediction power for different noise level (a, b, c) Submerged sphere in surge motion for  $T_e = 6.5$  s,  $T_e = 9.5$  s and  $T_e = 12.5$  s, respectively. (d, e, f) Submerged sphere in heave motion for  $T_e = 6.5$  s,  $T_e = 9.5$  s and  $T_e = 12.5$  s, respectively. (g, h, i) Floating sphere in surge motion for  $T_e = 6.5$  s,  $T_e = 9.5$  s and  $T_e = 12.5$  s, respectively. (j, k, l) Floating sphere in heave motion for  $T_e = 6.5$  s,  $T_e = 9.5$  s and  $T_e = 12.5$  s, respectively. (m, n, o) Bottom-hinged flap with zero pitch angle for  $T_e = 6.5$  s,  $T_e = 9.5$  s and  $T_e = 12.5$  s, respectively. (p, q, r) Bottom-hinged flap with  $-30^\circ$  pitch angle for  $T_e = 6.5$  s,  $T_e = 9.5$  s and  $T_e = 12.5$  s, respectively



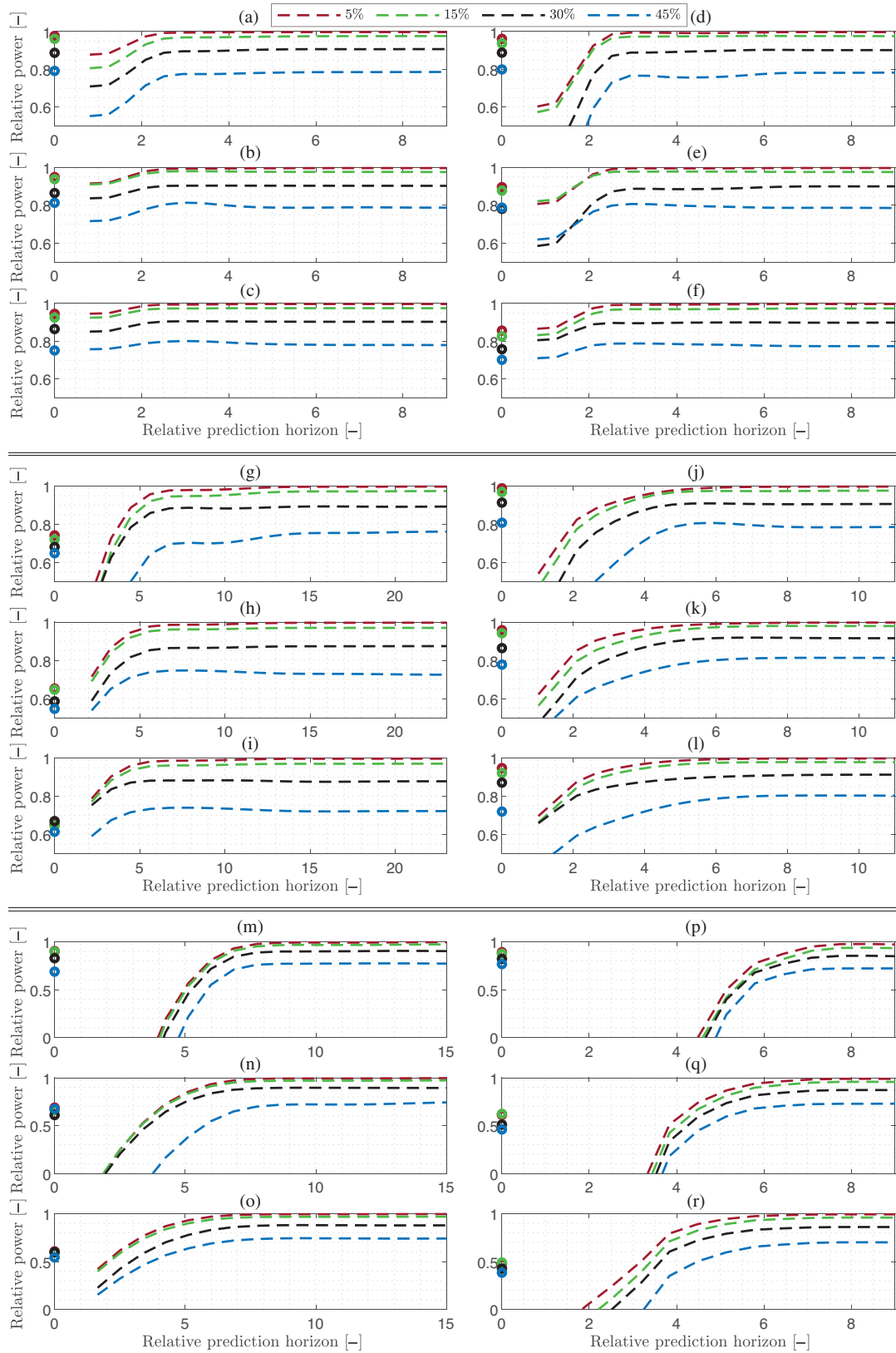


**FIGURE 16** Relative power versus prediction horizon for different noise levels for all concepts. Circles show the no-prediction power corresponding to each noise level. (a, b, c) Submerged sphere in surge motion for damping of 25 kNs/m and for  $T_e = 6.5$  s,  $T_e = 9.5$  s and  $T_e = 12.5$  s, respectively. (d, e, f) Submerged sphere in heave motion for damping of 25 kNs/m and for  $T_e = 6.5$  s,  $T_e = 9.5$  s and  $T_e = 12.5$  s, respectively. (g, h, i) Floating sphere in surge motion for damping of 25 kNs/m and for  $T_e = 6.5$  s,  $T_e = 9.5$  s and  $T_e = 12.5$  s, respectively. (j, k, l) Floating sphere in heave motion for damping of 25 kNs/m and for  $T_e = 6.5$  s,  $T_e = 9.5$  s and  $T_e = 12.5$  s, respectively. (m, n, o) Bottom-hinged flap with zero pitch angle for damping of 10 MNsm and for  $T_e = 6.5$  s,  $T_e = 9.5$  s and  $T_e = 12.5$  s, respectively. (p, q, r) Bottom-hinged flap with  $-30^\circ$  pitch angle for damping of 10 MNsm and for  $T_e = 6.5$  s,  $T_e = 9.5$  s and  $T_e = 12.5$  s, respectively

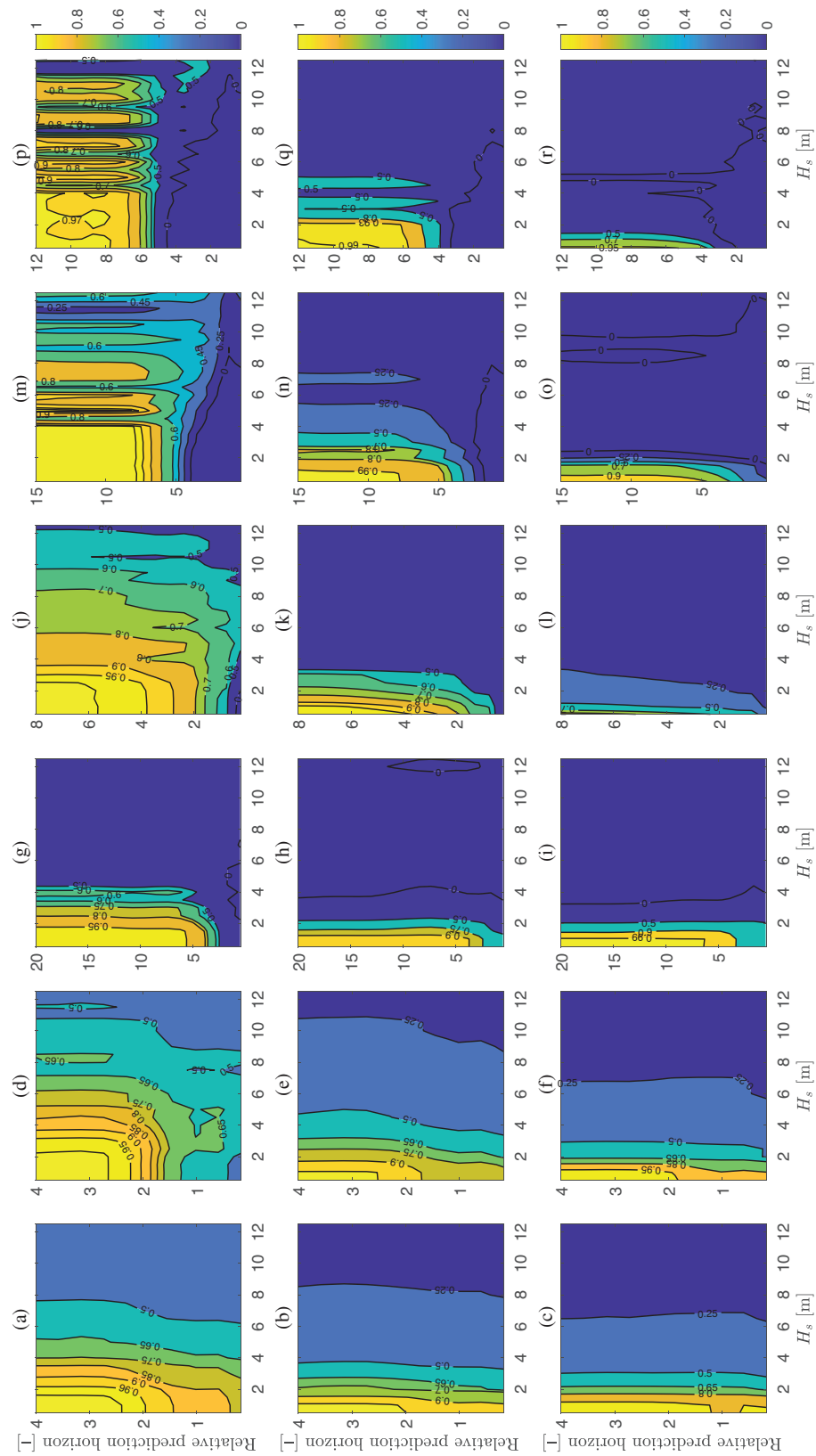


**FIGURE 17** Relative power as function of prediction horizon and significant wave height when amplitude constraints are applied. (a, b, c) Submerged sphere in surge motion for damping of 25 kNs/m and for  $T_e = 6.5$  s,  $T_e = 9.5$  s and  $T_e = 12.5$  s, respectively. (d, e, f) Submerged sphere in heave motion for damping of 25 kNs/m and for  $T_e = 6.5$  s,  $T_e = 9.5$  s and  $T_e = 12.5$  s, respectively. (g, h, i) Floating sphere in surge motion for damping of 25 kNs/m and for  $T_e = 6.5$  s,  $T_e = 9.5$  s and  $T_e = 12.5$  s, respectively. (j, k, l) Floating sphere in heave motion for damping of 25 kNs/m and for  $T_e = 6.5$  s,  $T_e = 9.5$  s and  $T_e = 12.5$  s, respectively. (m, n, o) Bottom-hinged flap with zero pitch angle for damping of 10 MNsm and for  $T_e = 6.5$  s,  $T_e = 9.5$  s and  $T_e = 12.5$  s, respectively. (p, q, r) Bottom-hinged flap with  $-30^\circ$  pitch angle for damping of 10 MNsm and for  $T_e = 6.5$  s,  $T_e = 9.5$  s and  $T_e = 12.5$  s, respectively

## 4.7 | Sensitivity to filtering

One way to reduce the prediction requirement is by filtering the optimal transfer function. Figure 18 demonstrates the effect of the filtering on prediction requirement. The prediction requirement becomes more sensitive to the filtering limit when the cut-off frequencies are placed in the slope of the transfer function. Starting at low wave frequency,  $\omega_e = 2\pi/T_e$ , the peak of the excitation spectrum shifts relatively towards lower frequencies as the wave period increases. For the submerged sphere in surge and heave motion at wave period of 12.5 s, the cut-off frequencies would be located around the non-steep beginning of the transfer function, which results in insensitivity to the filtering limit. A similar trend is seen for the floating sphere in surge motion. Contrarily, for the floating sphere in heave motion at  $T_e = 6.5$  s, the main content of the excitation spectral density falls around the trough of the transfer function, and consequently, low sensitivity to the filtering limit is seen. This also implies that the transfer function is nearly constant in the frequency range of importance, and that the prediction becomes unimportant: The control problem is close to causal in this particular sea state. On the other hand, for the sea states with  $T_e = 9.5$  s and 12.5 s, the cut-off frequencies are in the slope of the transfer function for this generic concept, hence, more sensitivity to the filtering limit is observed.

Another factor in defining the sensitivity to filtering limit is the shape of the excitation spectral density. In a steep spectrum, a change in filtering limit gives smaller variation in the cut-off frequencies. This effect contributes to the low sensitivity to filtering limit in high wave periods for the bottom-hinged flap.

A careful observation of the tail of the curves for different filtering limit reveals that the lines with higher filtering percentage converge towards a lower relative power at long prediction horizon, although the drop is quite small. Note that the results are presented with normalization based on the optimal power with an unfiltered transfer function.

## 5 | DISCUSSION

As expected from (22), the average optimal power shows a descending pattern when the relative damping is increased (see Figure 11). Not only does larger losses mean that a larger part of the absorbed power is dissipated, it also leads to a reduction of the optimal velocity, which again gives a reduction in the power absorbed from the wave. Referring to the recently published guidance from IEA-OES [34], one could say that minimising losses in the wave energy converter has double importance: Not only does it increase the power conversion efficiency; it also increases the power capture itself.

The contour plots in Figure 12 indicate that a low relative power is obtained for very small damping and short prediction horizon. An increase in loss damping implies that the transfer function becomes less dependant on the radiation resistance. When the loss damping becomes dominating (relative damping  $\gg 1$ ), the transfer function tends to a constant value, and as a

result, the need for prediction is removed and the control problem becomes causal. This is exemplified by Figure 19, where the difference between the sub-optimal and optimal velocity becomes negligible at high relative damping.

In most cases, the prediction horizon required to reach a certain level of power output, say relative power of 0.95, is similar across sea states for the same generic concept (Figure 13). In control theory terms, as argued by Fusco and Ringwood [6], the lowest characteristic frequency of the optimal transfer function is the dominant factor in defining the non-causality of the optimal velocity. A small lowest characteristic frequency implies a large time constant, and as a result,  $k_{\text{opt}}(t)$  slowly approaches zero. This puts a more demanding requirement on the prediction horizon for achieving the same relative power.

The shape of the curves seen in Figure 13 for low values of prediction horizon may be understood by looking at the impulse responses (Figure 7). When the length of the prediction horizon is close to the time  $\tau_0$  corresponding to the first zero-crossing of the impulse response function, the marginal increase in the information provided by an increased horizon is not made use of in the convolution of (15) due to the function value being close to zero. Since we have normalised the prediction horizon by  $\tau_0$  this leads to flat sections on the curves around relative prediction horizon equal to 1.

Filtering of the optimal transfer function has been shown to strongly increase performance in situations where the available prediction horizon is limited and the transfer function is sloped around the filtering frequency. If the excitation spectrum is at the same time centred at this sloping frequency range of the optimal transfer function, the filtering will however not be able to bring the performance close to the maximum absorption. It is therefore true to state that, unless the radiation resistance, and thereby the optimal transfer function, is fairly constant across the range of wave frequencies expected at the location of installation, a well-performing wave energy converter where losses have been minimised will depend on prediction: Filtering can strongly reduce the prediction need in some wave conditions, but not in all. This also means that the better the design is in terms of minimising losses, the more important the prediction will be in the wave conditions where filtering does not work well.

Note that the filtering has a similar effect to increased level of dissipative loss: They both reduce the variation of the transfer function, and thereby the need for prediction. Filtering may also be seen as a step towards making the transfer function causal, and then it should not come as a surprise that the power output converges to the no-prediction result when the filtering limits are increased (cf. Figure 18).

In [6], the loss coefficient was not varied but, according to the figures presented in the paper, chosen with a constant value of 100 Ns/m. With technology known today, it seems unrealistic that such low levels of loss can be reached for wave energy converters of the size being discussed. The range chosen for the loss damping in the present study is expected to cover the range achievable for a real system. The results that have just been presented therefore further relax the requirement on prediction horizon compared to what was achieved in [6] by the filtering approach. Although there are differences across concepts,

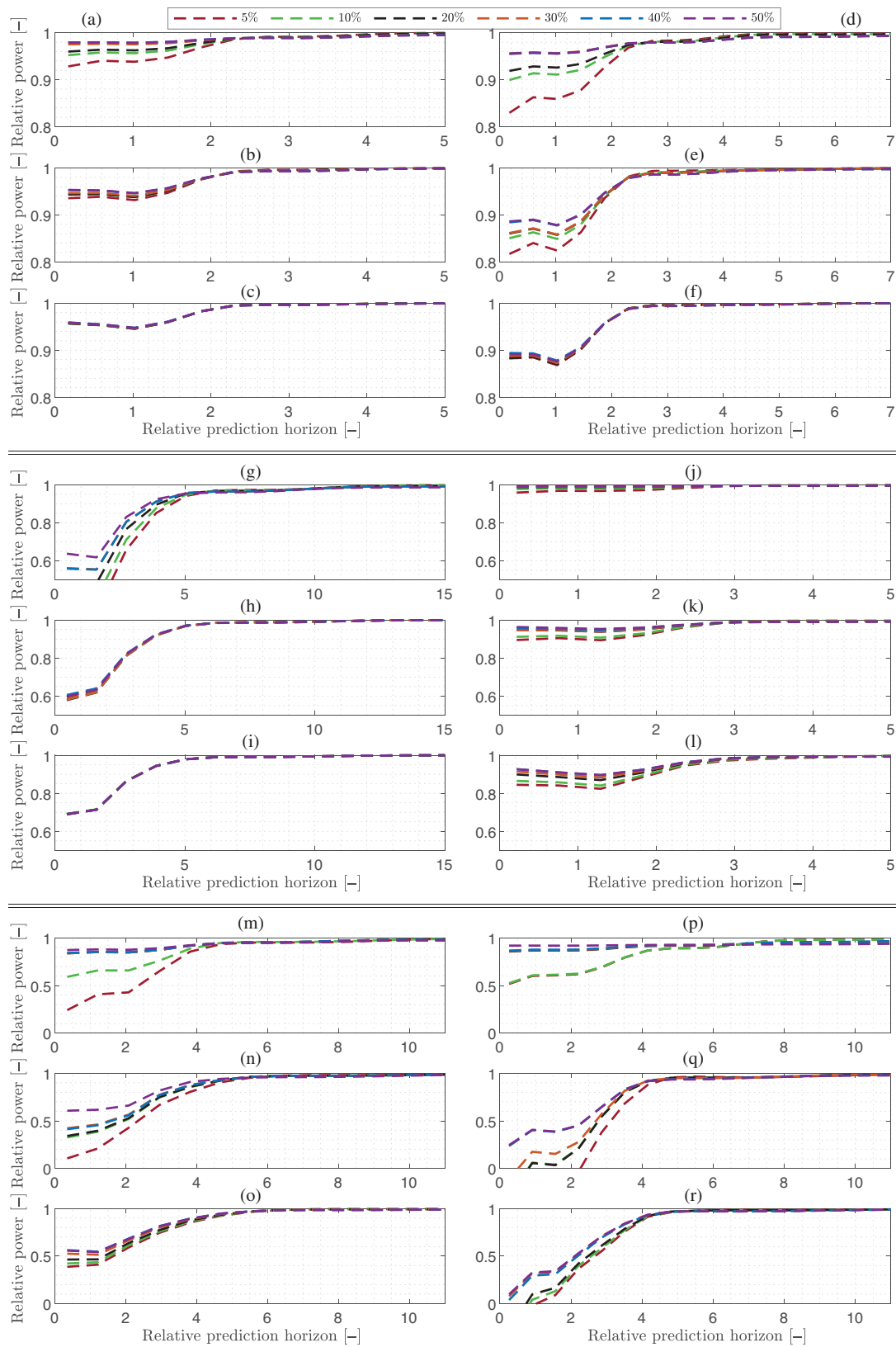


**FIGURE 18** Relative power versus prediction horizon, showing the effect of filtering of the transfer function at different filtering limits in the range 5–50%. (a, b, c) Submerged sphere in surge motion for damping of 25 kNs/m and for  $T_e = 6.5$  s,  $T_e = 9.5$  s and  $T_e = 12.5$  s, respectively. (d, e, f) Submerged sphere in heave motion for damping of 25 kNs/m and for  $T_e = 6.5$  s,  $T_e = 9.5$  s and  $T_e = 12.5$  s, respectively. (g, h, i) Floating sphere in surge motion for damping of 25 kNs/m and for  $T_e = 6.5$  s,  $T_e = 9.5$  s and  $T_e = 12.5$  s, respectively. (j, k, l) Floating sphere in heave motion for damping of 25 kNs/m and for  $T_e = 6.5$  s,  $T_e = 9.5$  s and  $T_e = 12.5$  s, respectively. (m, n, o) Bottom-hinged flap with zero pitch angle for damping of 10 MNsm and for  $T_e = 6.5$  s,  $T_e = 9.5$  s and  $T_e = 12.5$  s, respectively. (p, q, r) Bottom-hinged flap with  $-30^\circ$  pitch angle for damping of 10 MNsm and for  $T_e = 6.5$  s,  $T_e = 9.5$  s and  $T_e = 12.5$  s, respectively



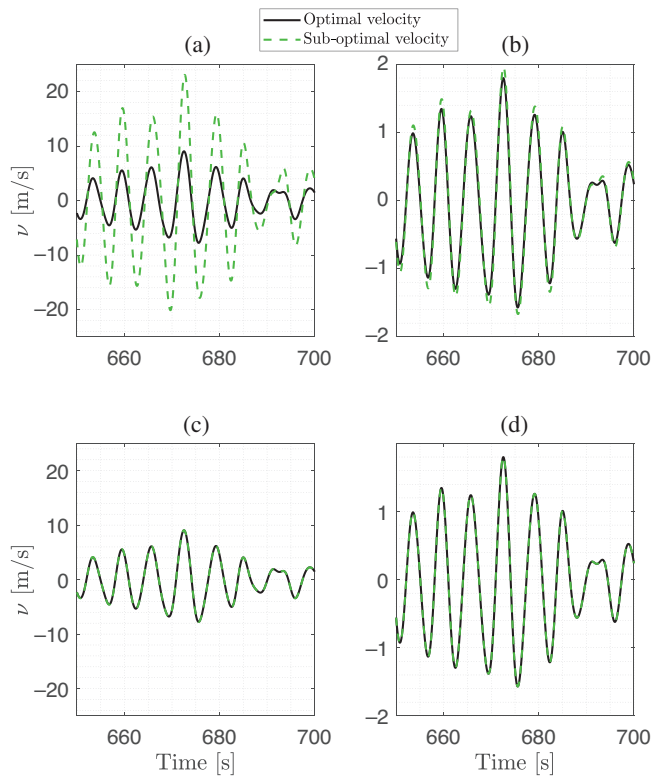


**FIGURE 19** Example of velocity time series for  $T_c = 6.5$  s and comparing the sub-optimal velocity result (dashed) with prediction horizon to the optimal velocity for the submerged sphere in surge. (a) For relative damping of 0.25 and relative prediction horizon of 0.17. (b) For relative damping of 0.25 and relative prediction horizon of 12.53. (c) For relative damping of 4.99 and relative prediction horizon of 0.17. (d) For relative damping of 4.99 and relative prediction horizon of 12.53

it may be stated that for an unconstrained system behaving fairly linearly, predicting a few seconds ahead will in general be sufficient for a properly designed optimal controller.

These good news on modest prediction need comes with a downside: The maximum achievable power output with a real system is significantly smaller than what is usually quoted as the maximum output for a wave energy converter, (21). Even with perfect control and unconstrained motion, the losses in the system push the maximum power down the curve represented by (22), which is steepest at the beginning as illustrated in Figure 11. The results presented for maximum power as function of energy period (Figure 14) further demonstrated this effect. Unless comparable in size to the wave length, concepts that are based on differences in hydrodynamic pressure, like submerged rigid bodies and those with surge-based excitation, are more exposed to this effect than concepts that find their forcing through difference between the hydrodynamic pressure and a constant pressure. In any case: Accurate identification of the loss damping is essential for a realistic assessment of the power output expected for a wave energy converter.

All results in this paper are derived based on idealised concepts working in one degree of freedom. For more realistic situations where the wave energy converter moves in several degrees of freedom, and energy is harvested through one or

more of them, the results derived here still apply to each of the rigid-body modes. A controller for a concept working, e.g. in both heave and surge will have to handle the problem as a combination of excitation and radiation in both modes, and consider how dissipative losses in the system influence each of them. But the overall prediction requirements are not expected to be any different from the combination of heave and surge results as derived in the present study.

Regarding the noise sensitivity, for all concepts, a noise level of up to 20% can be allowed without losing more than 10% of the optimal predicted power. In a real situation, the prediction is expected to be more accurate for earlier parts of the prediction horizon. This effect is not captured in the present study, but the results could be interpreted as a worst-case situation for uncertainty level evaluated at the end of the prediction horizon.

Note that the approach taken to compute the constrained sub-optimal power output for varying prediction horizon implies that the controller has to stop the motion when the constraint is reached, and then release again at the right moment. Depending on the machinery and its capacity, the controller might have to plan for this well ahead, in order not to spill power or cause detrimental end-stop impacts. It may be expected that this planning will require wave prediction about one half wave cycle ahead, such that the machinery capacity can be used most efficiently over the stroke. Whether a real machinery under constrained optimal control would perform worse or better than indicated by the simple representation of amplitude constraints used here would depend on the force (or torque) and power limitations of the machinery, but it is well known from other studies that amplitude-constraints typically lead to a similar latching-like behaviour that increases the amplitude of the fundamental harmonic component (see, e.g. [19]).

In the interpretation and use of the obtained results, it must be remembered that the model of the system has been fully linearised for all generic concepts. A real system is likely to have important non-linearities in its dynamic response, which will influence the optimal trajectory. It is plausible that such non-linearities will lead to the need of predicting the wave forces over the next half cycle or so to be able to reach the real optimum.

How the control to impose the optimal velocity is done is not considered in this work. With a reference-following approach, the computations done here could be used directly as an input to the machinery control system, as demonstrated in [6]. The results for required prediction horizon would also be implicitly valid for other implementations of optimal control. Yet there could be other control objectives such as load mitigation, minimised power fluctuations or production-on-demand, which would influence prediction requirements. Again it is expected that the corresponding requirement on the prediction horizon would, at maximum, be close to half a wave cycle.

## 6 | CONCLUSION

The maximum power output from wave energy converters as function of length of prediction horizon and level of dissipative losses has been investigated. The effect of other factors such

as energy period and spectrum shape factor, amplitude constraints, prediction accuracy and filtering of the transfer function for optimal velocity were also considered. Generic converter concepts made as combination of different body shapes, submergence levels and oscillation modes were studied and the assumption of linear behaviour has been used throughout.

Single truncation of the convolution integral for optimal velocity, i.e. applying the finite prediction horizon only on the non-causal side, utilises more available information than double truncation, and in general therefore results in higher power output. Single truncation was therefore used throughout the study.

The results show that dissipative losses like hydrodynamic drag and machinery friction reduce the need for prediction, and that with realistic assumptions for the level of such losses, predicting wave forces only a few seconds ahead is typically enough to obtain an accurate estimate of the optimal velocity and thereby reach the maximum power output in sea states where amplitude constraints are not reached. It is also found that for most generic concepts it is possible to reach at least 70% of the maximum absorbed power by properly choosing the transfer function as a constant in each sea state, which means the need for prediction is removed.

Within the range of variation studied for the peakness factor of the JONSWAP spectrum, namely,  $\gamma \in [1, 5]$ , the results are practically insensitive to the bandwidth of the wave spectrum. In general, filtering the optimal transfer function as suggested by Fusco and Ringwood [6] substantially improves the power conversion for most concepts in most sea states when only a limited prediction horizon is available.

Furthermore, it was found that the performance is quite robust to noise in the estimated and predicted excitation force, where a noise level corresponding to 20% of the level of variation of the excitation force itself leads to only 10% reduction in the useful power.

An approximate approach was taken to study the effect of constraints on the oscillation amplitude, which showed that the larger the significant wave height (or the more constrained the system is), the less the benefit from predicting the excitation force far ahead.

The obtained results are expected to be qualitatively valid also in the case of non-linear losses and additional control objectives although these are likely to influence the optimal velocity significantly. In order to handle non-linearities, additional control objectives, amplitude limits and various other constraints in reality, it is expected that one has to predict wave forces about half a wave cycle ahead.

The results therefore indicate that with properly designed optimal controllers, it should be possible to approach the maximum achievable power output for real systems with much shorter prediction horizon, from a few seconds up to half a wave period, than has generally been assumed earlier, e.g. in [6], where horizon lengths of up to about 15 s were reported with filtered transfer functions for heaving buoys.

## ACKNOWLEDGEMENTS

Jørgen H. Todalshaug and CorPower Ocean AB acknowledge financing from the Swedish Energy Agency through the

Nextwave project. The research in this paper was also supported by the Swedish Research Council (Grant number 2020-03634).



## CONFLICT OF INTERESTS

The authors have declared no conflict of interest.

## DATA AVAILABILITY STATEMENT

Data available on request from the authors.

## ORCID

Zabra Shahroozi  <https://orcid.org/0000-0002-1165-5569>  
 Jørgen Hals Todalshaug  <https://orcid.org/0000-0001-9050-0313>

## REFERENCES

1. Falnes, J., Kurniawan, A.: *Ocean Waves and Oscillating Systems: Linear Interactions including Wave-Energy Extraction*, vol. 8. Cambridge University Press, Cambridge (2020)
2. Korde, U.A.: Control system applications in wave energy conversion. In: *Proceedings of OCEANS 2000 MTS/IEEE Conference and Exhibition (Cat. No. 00CH37158)*, vol. 3, pp. 1817–1824. IEEE (2000)
3. Falnes, J.: A review of wave-energy extraction. *Mar. struct.* 20(4), 185–201 (2007)
4. Korde, U.A., Ringwood, J.: *Hydrodynamic Control of Wave Energy Devices*. Cambridge University Press, Cambridge (2016)
5. Scruggs, J., Lattanzio, S., Taflanidis, A., Cassidy, I.: Optimal causal control of a wave energy converter in a random sea. *Appl. Ocean Res.* 42, 1–15 (2013)
6. Fusco, F., Ringwood, J.V.: A study of the prediction requirements in real-time control of wave energy converters. *IEEE Trans. Sustainable Energy* 3(1), 176–184 (2012)
7. Price, A., Forehand, D., Wallace, A.: Time-span of future information necessary for theoretical acausal optimal control of wave energy converters. In: *2009 European Control Conference (ECC)*, pp. 3761–3766. IEEE (2009)
8. Mérigaud, A., Ringwood, J.V.: Incorporating ocean wave spectrum information in short-term free-surface elevation forecasting. *IEEE J. Oceanic Eng.* 44(2), 401–414 (2018)
9. Fusco, F.: *Forecasting requirements in the optimal control of wave energy converters: Research Report* (2009)
10. Tedd, J., Frigaard, P., et al.: Short term wave forecasting, using digital filters, for improved control of wave energy converters. In: *The Seventeenth International Offshore and Polar Engineering Conference*. International Society of Offshore and Polar Engineers (2007)
11. Schoen, M.P., Hals, J., Moan, T.: Wave prediction and robust control of heaving wave energy devices for irregular waves. *IEEE Trans. Energy Convers.* 26(2), 627–638 (2011)
12. Ge, M., Kerrigan, E.C.: Short-term ocean wave forecasting using an autoregressive moving average model. In: *UKACC 11th International Conference on Control (CONTROL)*, pp. 1–6. IEEE (2016)
13. Paparella, F., Monk, K., Winands, V., Lopes, M., Conley, D., Ringwood, J.V.: Benefits of up-wave measurements in linear short-term wave forecasting for wave energy applications. In: *IEEE Conference on Control Applications (CCA)*, pp. 2048–2053. IEEE (2014)
14. Fusco, F., Ringwood, J.V.: Short-term wave forecasting for real-time control of wave energy converters. *IEEE Trans. Sustainable Energy* 1(2), 99–106 (2010)
15. Folley, M., Whittaker, T., van't Hoff, J.: The design of small seabed-mounted bottom-hinged wave energy converters. In: *Proceedings of the 7th European Wave and Tidal Energy Conference*, vol. 455 (2007)
16. Dias, F., Renzi, E., Gallagher, S., Sarkar, D., Wei, Y., Abadie, T., et al.: Analytical and computational modelling for wave energy systems: The example of oscillating wave surge converters. *Acta Mech. Sin.* 33(4), 647–662 (2017)

17. Folley, M., Whittaker, T.: Spectral modelling of wave energy converters. *Coastal Eng.* 57(10), 892–897 (2010)
18. Fusco, F., Gilloteaux, J.C., Ringwood, J.: A study on prediction requirements in time-domain control of wave energy converters. *IFAC Proc. Vol.* 43(20), 372–377 (2010)
19. Hals, J., Falnes, J., Moan, T.: A comparison of selected strategies for adaptive control of wave energy converters. *J. Offshore Mech. Arct. Eng.* 133(3), 031101 (2011)
20. Falnes, J.: On non-causal impulse response functions related to propagating water waves. *Appl. Ocean Res.* 17(6), 379–389 (1995)
21. Henry, A., Folley, M., Whittaker, T.: A conceptual model of the hydrodynamics of an oscillating wave surge converter. *Renewable Energy* 118, 965–972 (2018)
22. Lee, C., Newman, J.: *Wamit—User Manual Version 7.0*. Wamit (2013)
23. AeroHydro Inc.: *MultiSurf—User Manual Version 8.0*. AeroHydro Inc. (2011)
24. Cuttler, M.V., Hansen, J.E., Lowe, R.J.: Seasonal and interannual variability of the wave climate at a wave energy hotspot off the southwestern coast of Australia. *Renewable Energy* 146, 2337–2350 (2020)
25. Det Norske Veritas : Recommended practice DNV-RP-C205: environmental conditions and environmental loads. DNV, Norway (2010)
26. Ribeiro, A.S., deCastro, M., Rusu, L., Bernardino, M., Dias, J.M., Gomez-Gesteira, M.: Evaluating the future efficiency of wave energy converters along the NW coast of the Iberian Peninsula. *Energies* 13(14), 3563 (2020)
27. Silva, D., Soares, C.G.: Assessment of the wave power resource at Madeira archipelago with the SWAN model. In: *Developments in Renewable Energies Offshore: Proceedings of the 4th International Conference on Renewable Energies Offshore (RENEW 2020)*, 12–15 October 2020, Lisbon, Portugal, p. 45. CRC Press (2020)
28. Guo, B., Patton, R.J., Jin, S., Lan, J.: Numerical and experimental studies of excitation force approximation for wave energy conversion. *Renewable Energy* 125, 877–889 (2018)
29. Abdelrahman, M., Patton, R., Guo, B., Lan, J.: Estimation of wave excitation force for wave energy converters. In: *3rd Conference on Control and Fault-Tolerant Systems (SysTol)*, pp. 654–659. IEEE (2016)
30. Garcia-Abril, M., Paparella, F., Ringwood, J.V.: Excitation force estimation and forecasting for wave energy applications. *IFAC-PapersOnLine* 50(1), 14692–14697 (2017)
31. Kracht, P., Perez-Becker, S., Richard, J.B., Fischer, B.: Performance improvement of a point absorber wave energy converter by application of an observer-based control: Results from wave tank testing. *IEEE Trans. Ind. Appl.* 51(4), 3426–3434 (2015)
32. Ling, B.A.: Real-time estimation and prediction of wave excitation forces for wave energy control applications. Master's Thesis, Oregon State University (2015)
33. Mhatre, S. : Application of a linear optimal estimator on a wave energy converter using bang-singular-bang control. Master's Thesis, Michigan Technological University (2017)
34. Hodges, J., Henderson, J., Ruedy, L., Soede, M., Weber, J. & Ruiz-Minguela, P. et al.: An international evaluation and guidance framework for ocean energy technology. IEA-OES (2021)

**How to cite this article:** Shahroozi, Z., Götteman, M., Engström, J., Todalshaug, J.H. Considerations on prediction horizon and dissipative losses for wave energy converters. *IET Renew. Power Gener.* 15, 3434–3458 (2021). <https://doi.org/10.1049/rpg.2.12290>

## APPENDIX: SENSITIVITY TO SPECTRAL SHAPE FACTOR

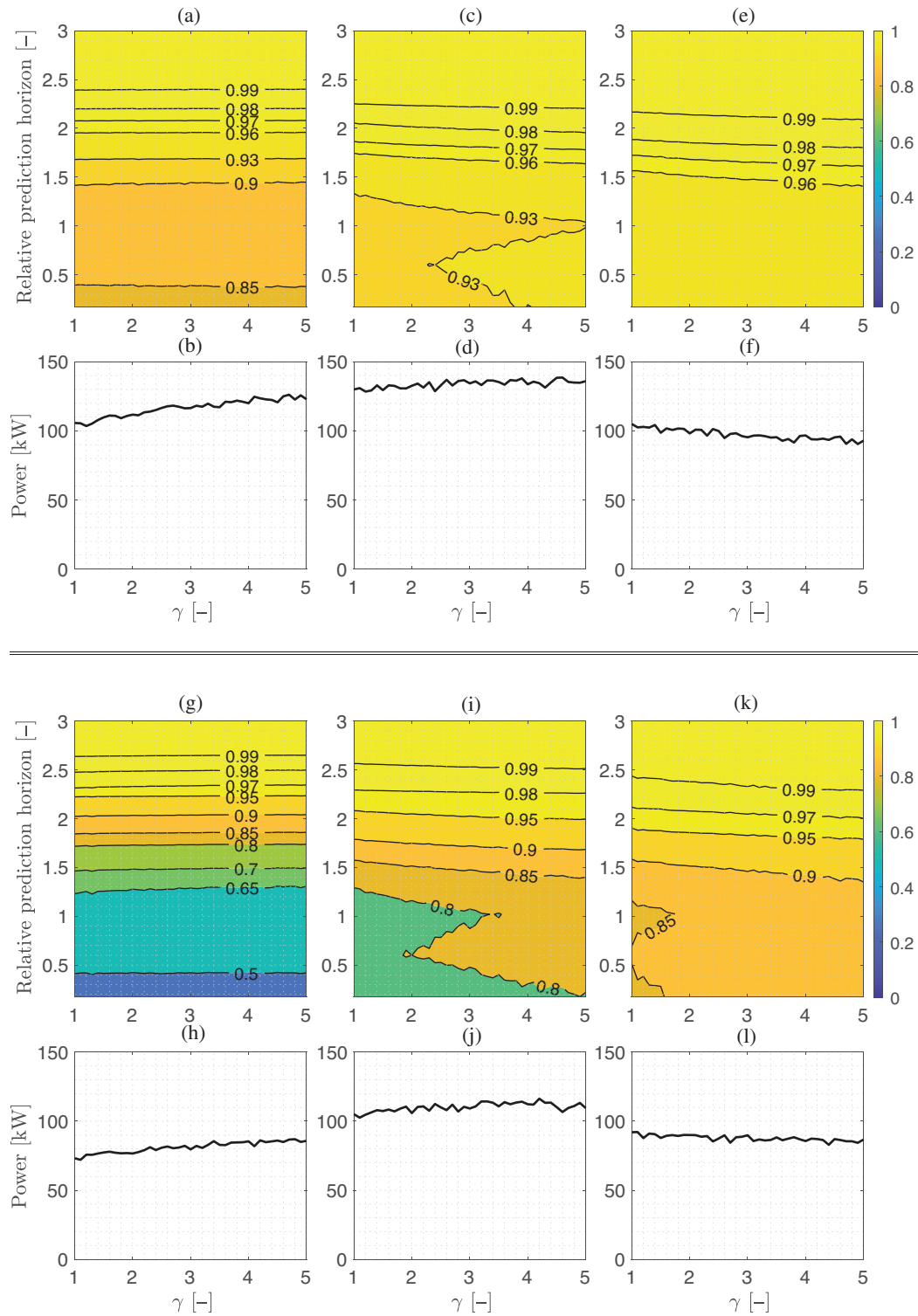


**FIGURE A.1** Sensitivity of prediction horizon to the JONSWAP shape factor,  $\gamma$ , for submerged sphere in both surge and heave motion and for damping of 25 kNs/m. (a) Contour plot of the relative power for relative prediction horizon and shape factor, for submerged sphere in surge motion and for  $T_e = 6.5$  s. (b) Optimal power versus shape factor, for submerged sphere in surge motion and for  $T_e = 6.5$  s. (c) Contour plot of the relative power for relative prediction horizon and shape factor, for submerged sphere in surge motion and for  $T_e = 9.5$  s. (d) Optimal power versus shape factor, for submerged sphere in surge motion and for  $T_e = 9.5$  s. (e) Contour plot of the relative power for relative prediction horizon and shape factor, for submerged sphere in surge motion and for  $T_e = 12.5$  s. (f) Optimal power versus shape factor, for submerged sphere in surge motion and for  $T_e = 12.5$  s. (g) Contour plot of the relative power for relative prediction horizon and shape factor, for submerged sphere in heave motion and for  $T_e = 6.5$  s. (h) Optimal power versus shape factor, for submerged sphere in heave motion and for  $T_e = 6.5$  s. (i) Contour plot of the relative power for relative prediction horizon and shape factor, for submerged sphere in heave motion and for  $T_e = 9.5$  s. (j) Optimal power versus shape factor, for submerged sphere in heave motion and for  $T_e = 9.5$  s. (k) Contour plot of the relative power for relative prediction horizon and shape factor, for submerged sphere in heave motion and for  $T_e = 12.5$  s. (l) Optimal power versus shape factor, for submerged sphere in heave motion and for  $T_e = 12.5$  s



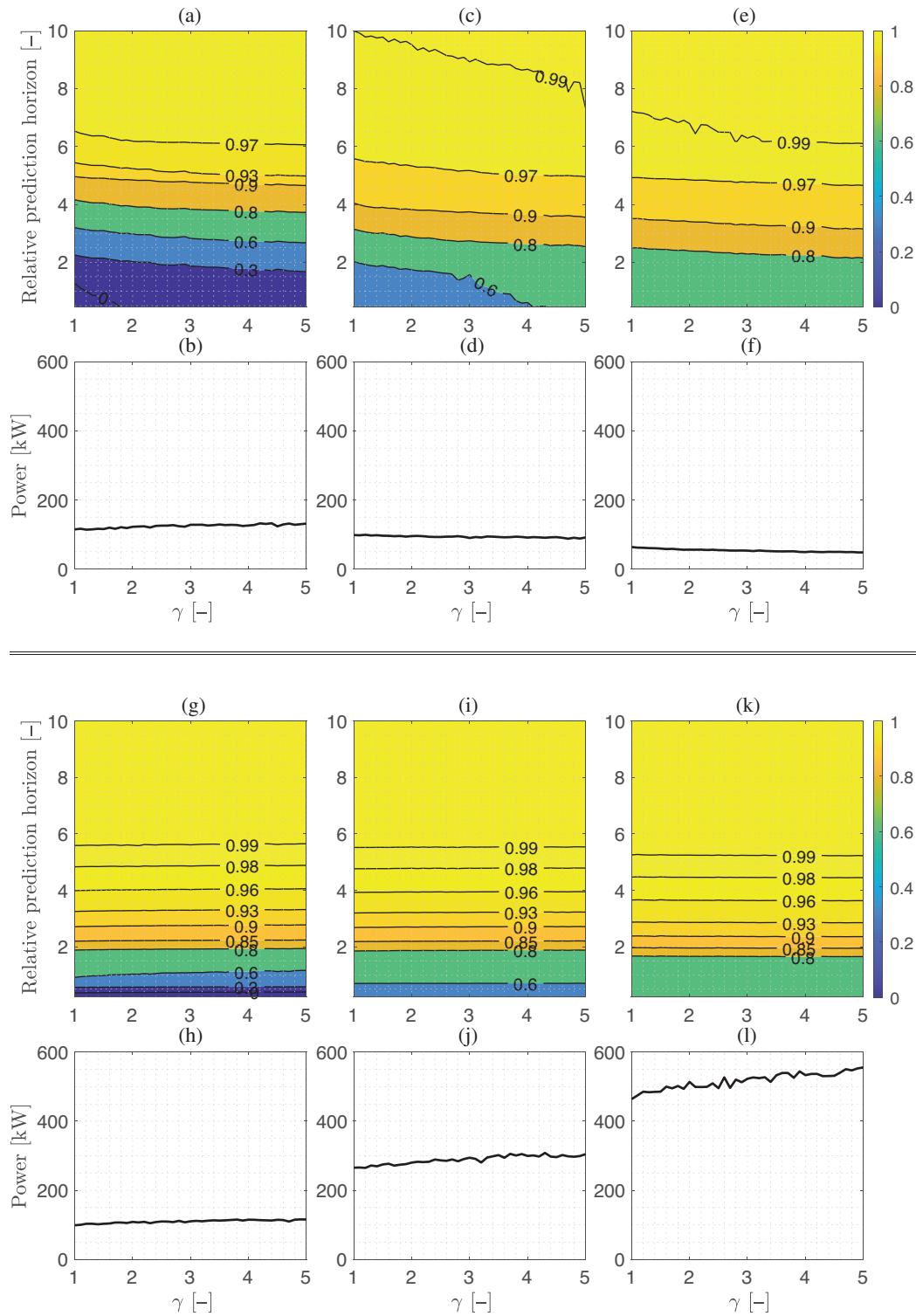


**FIGURE A.2** Sensitivity of prediction horizon to the JONSWAP shape factor,  $\gamma$ , for floating sphere in both surge and heave motion and for damping of 25 kNs/m. (a) Contour plot of the relative power for relative prediction horizon and shape factor, for floating sphere in surge motion and for  $T_e = 6.5$  s. (b) Optimal power versus shape factor, for floating sphere in surge motion and for  $T_e = 6.5$  s. (c) Contour plot of the relative power for relative prediction horizon and shape factor, for floating sphere in surge motion and for  $T_e = 9.5$  s. (d) Optimal power versus shape factor, for floating sphere in surge motion and for  $T_e = 9.5$  s. (e) Contour plot of the relative power for relative prediction horizon and shape factor, for floating sphere in surge motion and for  $T_e = 12.5$  s. (f) Optimal power versus shape factor, for floating sphere in surge motion and for  $T_e = 12.5$  s. (g) Contour plot of the relative power for relative prediction horizon and shape factor, for floating sphere in heave motion and for  $T_e = 6.5$  s. (h) Optimal power versus shape factor, for floating sphere in heave motion and for  $T_e = 6.5$  s. (i) Contour plot of the relative power for relative prediction horizon and shape factor, for floating sphere in heave motion and for  $T_e = 9.5$  s. (j) Optimal power versus shape factor, for floating sphere in heave motion and for  $T_e = 9.5$  s. (k) Contour plot of the relative power for relative prediction horizon and shape factor, for floating sphere in heave motion and for  $T_e = 12.5$  s. (l) Optimal power versus shape factor, for floating sphere in heave motion and for  $T_e = 12.5$  s

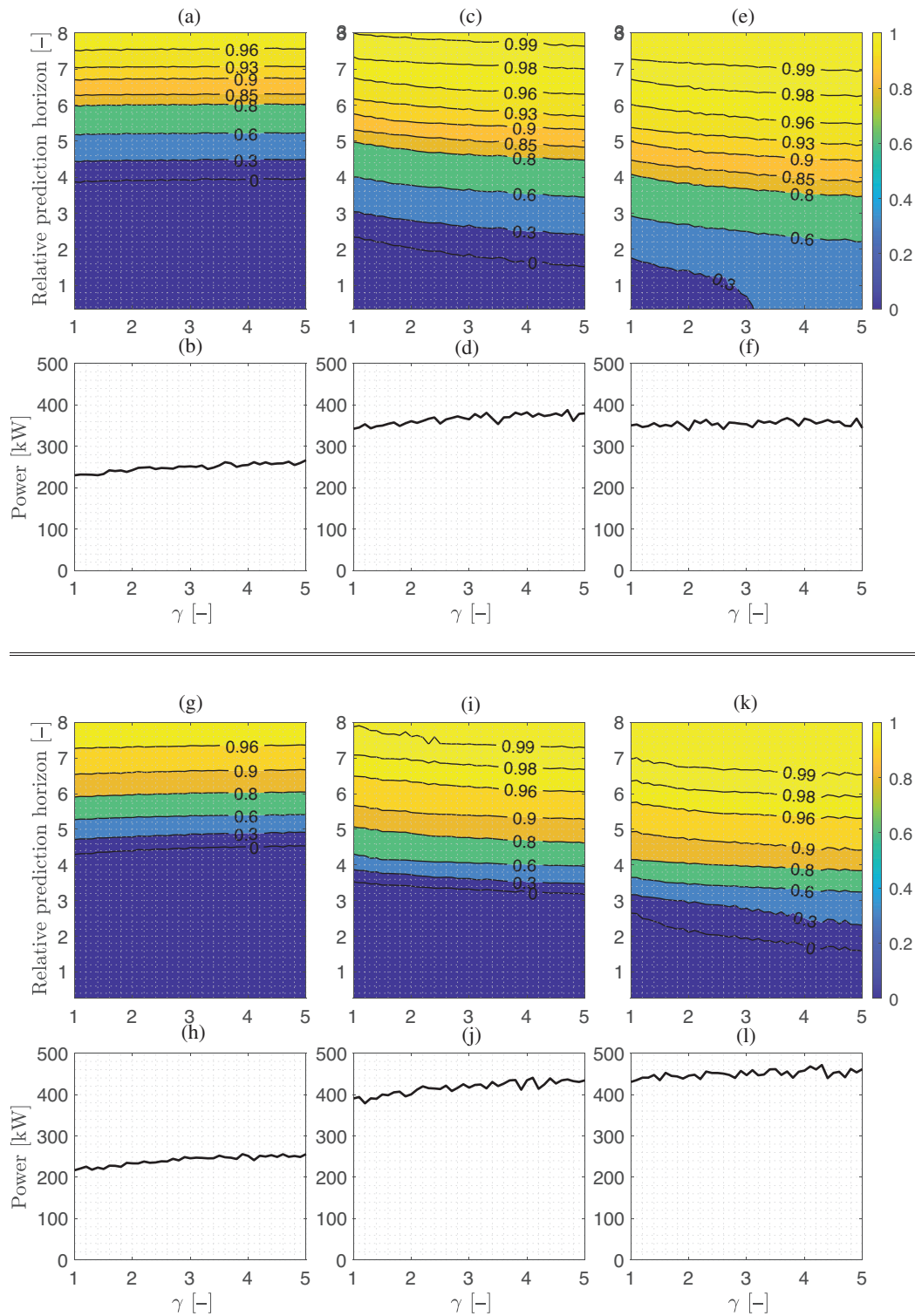


**FIGURE A.3** Sensitivity of prediction horizon to the JONSWAP shape factor,  $\gamma$ , for bottom-hinged flap for both zero and  $-30^\circ$  pitch angle and for damping of 10 MNsm (a) Contour plot of the relative power for relative prediction horizon and shape factor, for bottom-hinged flap with zero pitch angle and for  $T_e = 6.5$  s. (b) Optimal power versus shape factor, for bottom-hinged flap with zero pitch angle and for  $T_e = 6.5$  s. (c) Contour plot of the relative power for relative prediction horizon and shape factor, for bottom-hinged flap with zero pitch angle and for  $T_e = 9.5$  s. (d) Optimal power versus shape factor, for bottom-hinged flap with zero pitch angle and for  $T_e = 9.5$  s. (e) Contour plot of the relative power for relative prediction horizon and shape factor, for bottom-hinged flap with zero pitch angle and for  $T_e = 12.5$  s. (f) Optimal power versus shape factor, for bottom-hinged flap with zero pitch angle and for  $T_e = 12.5$  s. (g) Contour plot of the relative power for relative prediction horizon and shape factor, for bottom-hinged flap with  $-30^\circ$  pitch angle and for  $T_e = 6.5$  s. (h) Optimal power versus shape factor, for bottom-hinged flap with  $-30^\circ$  pitch angle and for  $T_e = 6.5$  s. (i) Contour plot of the relative power for relative prediction horizon and shape factor, for bottom-hinged flap with  $-30^\circ$  pitch angle and for  $T_e = 9.5$  s. (j) Optimal power versus shape factor, for bottom-hinged flap with  $-30^\circ$  pitch angle and for  $T_e = 9.5$  s. (k) Contour plot of the relative power for relative prediction horizon and shape factor, for bottom-hinged flap with  $-30^\circ$  pitch angle and for  $T_e = 12.5$  s. (l) Optimal power versus shape factor, for bottom-hinged flap with  $-30^\circ$  pitch angle and for  $T_e = 12.5$  s